HIGH GRADE CONTROL OF LINEAR INDUCTION MOTOR DRIVES

by

HAIDONG YU

Presented to the Faculty of the Graduate School of
The University of Texas at Arlington in Partial Fulfillment
of the Requirements
for the Degree of

DOCTOR OF PHILOSOPHY

THE UNIVERSITY OF TEXAS AT ARLINGTON

December 2007

ACKNOWLEDGEMENTS

I am sincerely grateful to my supervisor Dr. Babak Fahimi for his supervision and support. His guidance and encouragement has been vital to my learning. I thank him for mentoring me for completion of this dissertation.

I would like to thank Dr. Raymond R. Shoults, Dr. Wei-Jen Lee, Dr. Kai-Sing Yeung, and Dr. Soontorn Oraintara for being in my supervising committee. Their views and suggestions have been valuable for completeness of the dissertation.

I wish to thank all the members from the Power Electronics and Controlled Motion (PECM) Laboratory for the support in completion of this dissertation.

I also want to thank Dr. Steven D. Pekarek and Mr. Dezheng Wu from Purdue University for their cooperation with PECM lab.

Last but not least, my thanks are extended to my parents for their inexhaustible love and support to me. I also want to express my appreciation to Helen Huang for her encouragement and support.

November 14, 2007

ABSTRACT

HIGH GRADE CONTROL OF LINEAR INDUCTION MOTOR DRIVES

Publication No. ______

HAIDONG YU, PhD.

The University of Texas at Arlington, 2007

Supervising Professor: Babak Fahimi

Linear induction machines (LIM) have been widely utilized in military, transportation, and aerospace due to the impressive advantages such as simple configuration, easy maintenance, and high acceleration/deceleration. However, the existence of trailing eddy current effects and magnetic asymmetry effects undermines the expected functionality of vector control even though LIM possesses similarities from its rotary counterpart. As a result, it has been a focal research area to either improve the performance of vector control for LIM or develop a new high grade control strategy.

Therefore, the in-depth exploration of electromagnetic behavior of LIM has been a fundamental step for investigation of LIM. From both finite element analysis (FEA) and experiment, it is verified that the two open ends in the primary of LIM result in the magnetic asymmetry effects. Furthermore, both the trailing eddy current effects and magnetic asymmetry effects cause non-sinusoidal magneto-motive force (MMF). This undermines the basic assumption of vector control that the fundamental MMF should be sinusoidal. Moreover, FEA is a good tool for numerical-based analysis of electrical machines. However, the computational effort is extremely intensive. Therefore, the field reconstruction method (FRM) for LIM is proposed in this dissertation. FRM significantly reduces the computational time, but supplies steady state calculation in good accuracy. This dissertation also proposes a maximum force/ampere control, which has impressive advantages such as simple implementation, easy controllability, and maximum energy conversion ratio. The maximum force/ampere control is validated by both simulation results and experimental verification.

The contribution of this dissertation can be summarized as follows:

1. Systematic exploration of electromagnetic behavior of LIM;
2. Development of field reconstruction method for LIM;
3. Invention and implementation of maximum force/ampere control.

TABLE OF CONTENTS

Chapter

Appendix

LIST OF ILLUSTRATIONS

CHAPTER 1

INTRODUCTION

1.1 Background and Significance

The origin of linear electric machines can be traced back about one century ago. However, only after 1960, due to the occurrence of the modern power electronics technique, linear electric machines have attracted a great deal of interest. Linear electric machines can be conceptually realized by “cutting” and “unrolling” their counterpart, rotary electric machines. The process is illustrated by figure 1.

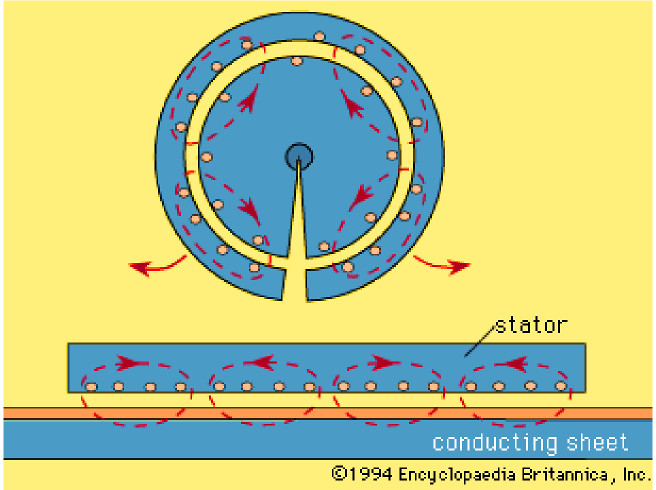

Figure 1 Imaginary Process of Obtaining Linear Electric Machines

From the aspect of electrical excitation, linear electric machines include linear dc machines, linear synchronous machines, linear induction machines, and linear step motors. With respect to geometry, linear electric machines have flat and tubular types.

The whole family of linear electric machines is classified in figure 2.

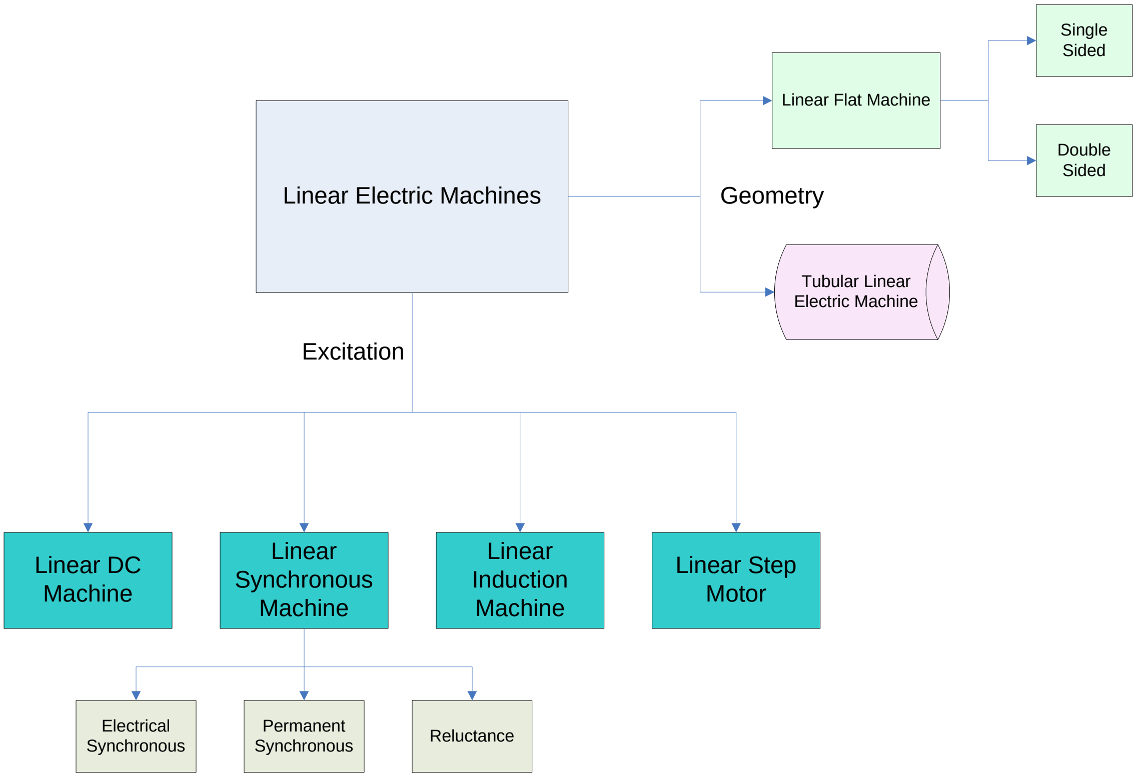

Figure 2 Classification of Linear Electric Machines

As one category of linear electric machines, linear induction machines (LIM) have been utilized in a wide range of applications [1]-[6] such as military, transportation, and aero space to name a few due to the impressive advantages such as simple configuration, easy maintenance, high propulsion, and no need for the transformation systems from rotary to translational movement. Figure 3 and 4 illustrate applications mentioned above. This dissertation will investigate single sided linear flat induction machine.

Figure 3 Air Train (From Wikipedia)

Figure 4 Nagahori Tsurumi-ryokuchi Line in Japan (From Wikipedia)

Conventionally, the moveable part of LIM is called primary, and the stationary part is called secondary. Primary usually contains a three phase winding in the uniform slots of the laminated core. Secondary is made of an aluminum (copper) sheet with (or without) a solid back iron core. Therefore, when the primary is excited by a set of balanced sinusoidal currents, there will be eddy current inducing on the secondary aluminum sheet. These two electromagnetic sources will react to produce electromagnetic forces. The tangential force is called thrust. The other component of force is called normal force.

1.2 Motivation and Technical Objectives

There are three most popular control strategies for linear induction motor drives. They are scalar control (V/F) [7] and [8], direct torque control (DTC) [9], and vector control [10]-[12]. Scalar control is also called Volt/Hertz control. It regulates the ratio of voltage with frequency at a constant value. Direct torque control uses errors between the references of primary flux and the force with their estimated values to determine the optimal switching configuration of the three phase inverter every sample time. Vector control includes direct field oriented control (DFOC) [11] and indirect field oriented control (IFOC) [13]. Vector control measures or estimates the location of rotor flux axis, and uses the flux angle to decouple the stator currents into quadrature and direct components, i.e. I_q and I_d. I_d is normally regulated at its rated value, and I_q is regulated to deliver commanded force. Since this family of machines possesses similarities with their rotary counterparts, vector control scheme is the most often used technique for LIM, and has been considered as the best control solution for LIM. Some other control strategies [13]-[15] based on vector control incorporate advanced control methods to improve the performance of LIM.

However, some electromagnetic behavior of LIM such as trailing eddy current effects [16]-[19] and magnetic asymmetry effects [20] and [21] can undermine the expected functionality of vector control. As a result, one can not harvest the high grade control performance from LIM using vector control. Therefore, the motivation of this dissertation is to develop and implement a high grade control scheme for LIM to achieve simple implementation, fast response, and maximum energy conversion ratio. Furthermore, the new invented control scheme, maximum force/ampere control, will be compared with the conventional IFOC both in simulation study and experimental test to illustrate its superior performance.

Development and implementation of a high grade control strategy for LIM has led to exploration of the complete understanding of electromagnetic behavior of LIM. In addition, finite element analysis (FEA) [22]-[25] is a widely used tool for numerical-based analysis of electrical machines. However, FEA requires intensive computational effort, which is not time efficient. Therefore, a new efficient field calculation technique, field reconstruction method (FRM) [26] and [27], is proposed to ease the investigation of LIM.

1.3 Contributions

The contributions of this dissertation can be summarized as:

1. Systematic exploration of electromagnetic behavior of LIM and discovery of shortcomings of vector control method in optimal control of LIM;
2. Development of field reconstruction method for LIM;
3. Invention and implementation of maximum force/ampere control.

CHAPTER 2

ELECTROMAGNETIC BEHAVIOR OF LINEAR INDUCTION MACHINES

In order to develop and implement a high grade control scheme for linear induction machine, in-depth knowledge of electromagnetic behavior is necessary. Finite element analysis (FEA) is used in this procedure.

2.1 LIM Model in FEA

Figure 5 shows the cross sectional view of the prototype in FEA based on the machine construction details. Commercially available package MagNet from Infolytica is used for this investigation. The primary winding scheme is shown in figure 6. The type of the winding is in ‘Star’ or ‘Y’ connection.

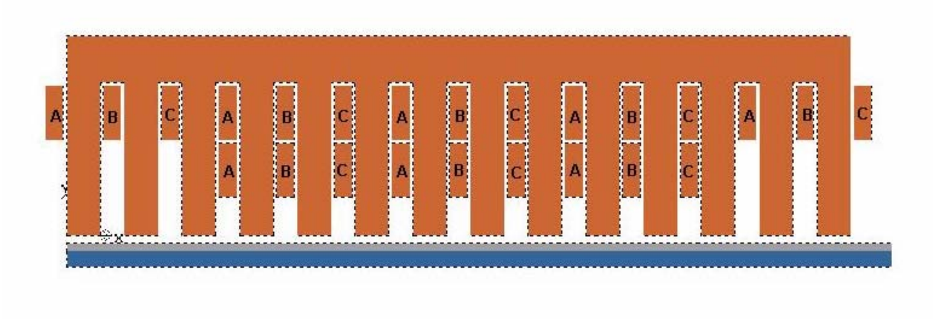

Figure 5 Cross Sectional View of LIM under Investigation

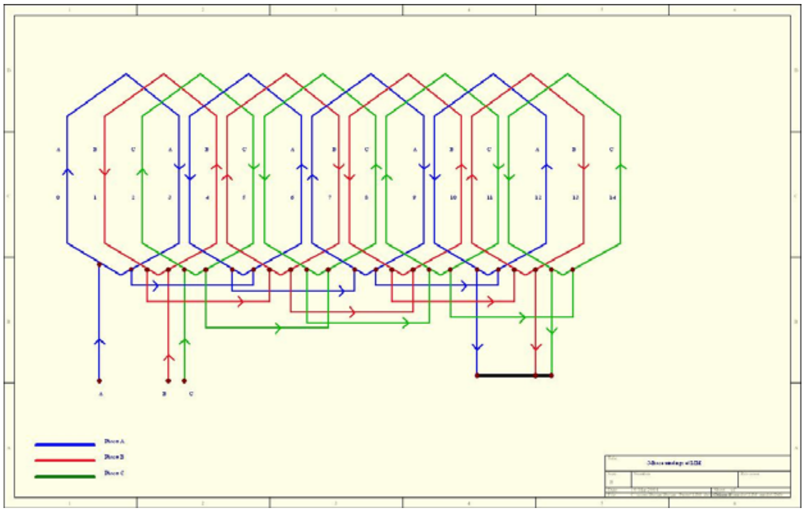

Figure 6 Primary Winding Scheme

Figure 7 illustrates the initial 2D mesh of LIM under investigation. The solver method in FEA is Newton-Raphson iteration method. The maximum iteration number is 20, and the polynomial order is 1. In order to guarantee the accuracy of FEA calculations, the maximum length of triangle sides located around the airgap, aluminum sheet surface, and primary teeth surface is about 1 mm.

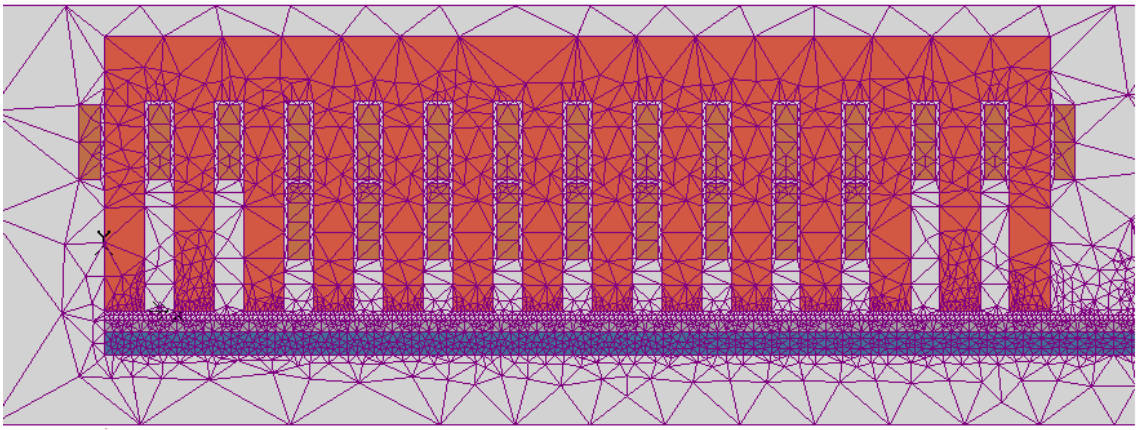

Figure 7 Initial 2D Mesh of LIM in FEA

2.2 Trailing Eddy Current Effects

As shown in figure 8, when linear induction machines move forward (from left to right), there is always eddy current that is not in the overlapped region between primary and secondary. This eddy current is called trailing eddy current. Trailing eddy current can cause non-sinusoidal and asymmetric magneto-motive force (*MMF*). These effects will undermine the proper functionality of conventional vector control of LIM.

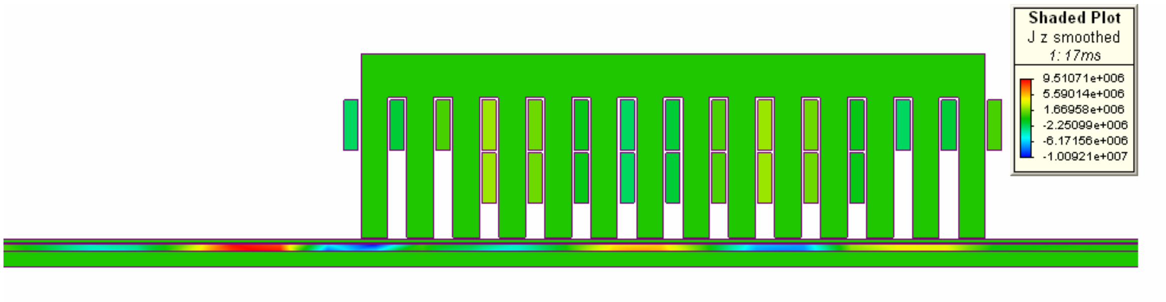

Figure 8 Trailing Eddy Current in FEA

2.3 Magnetic Asymmetry Effects

Unlike rotary induction machine, LIM has two open ends in primary. Due to different relative positions of phases *a*, *b*, and *c* in primary, the contribution of each phase to the *MMF* will be unequal. Figure 9, 10, and 11 illustrate the flux density distribution when phases *a*, *b*, and *c* are excited by a dc current respectively under lock up condition (direct method). The excitation circuit is shown in figure 12. One can notice that the peak flux densities in the primary in each case are 0.560416 T, 0.507523 T, and 0.582781 T in sequence. There is a significant difference in primary flux density between phase *b*, and phases *a* and *c*.

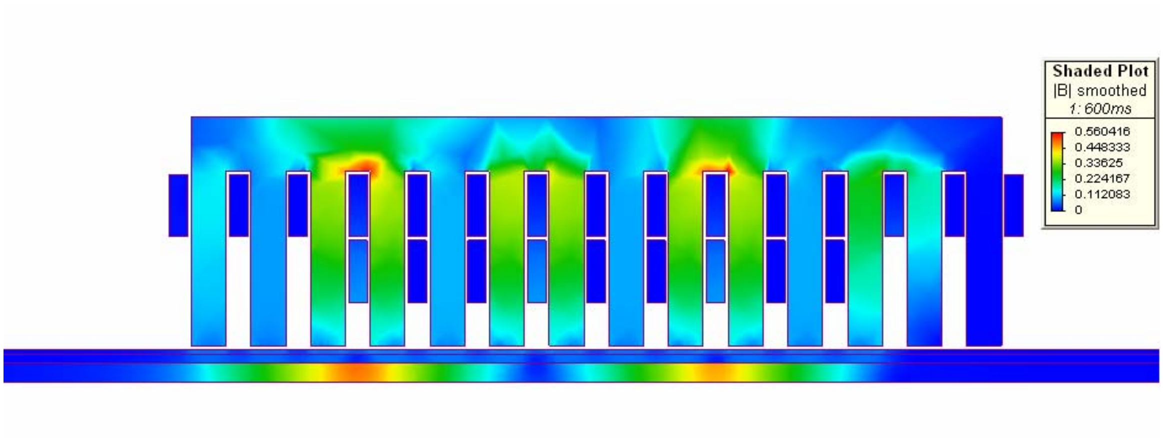

Figure 9 Flux Density Distribution when Phase a is Excited by a DC Current

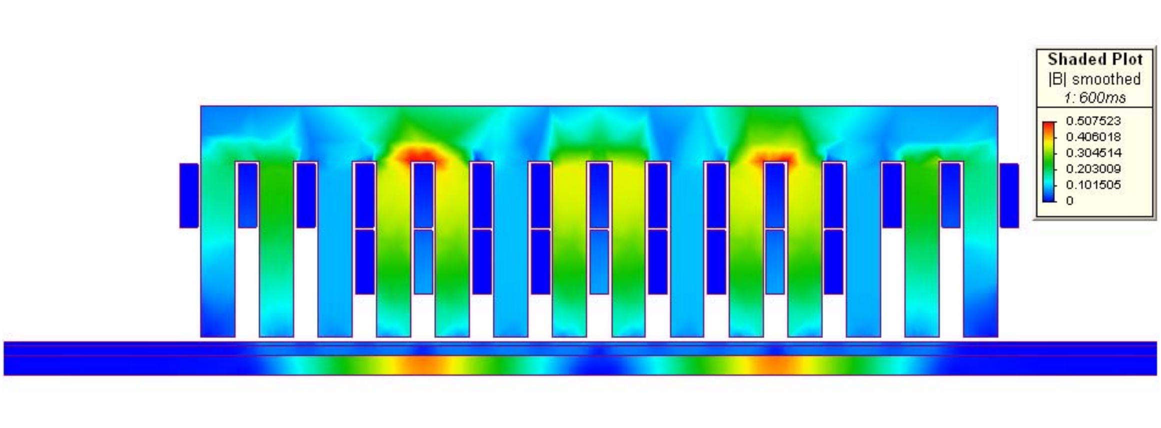

Figure 10 Flux Density Distribution when Phase b is Excited by a DC Current

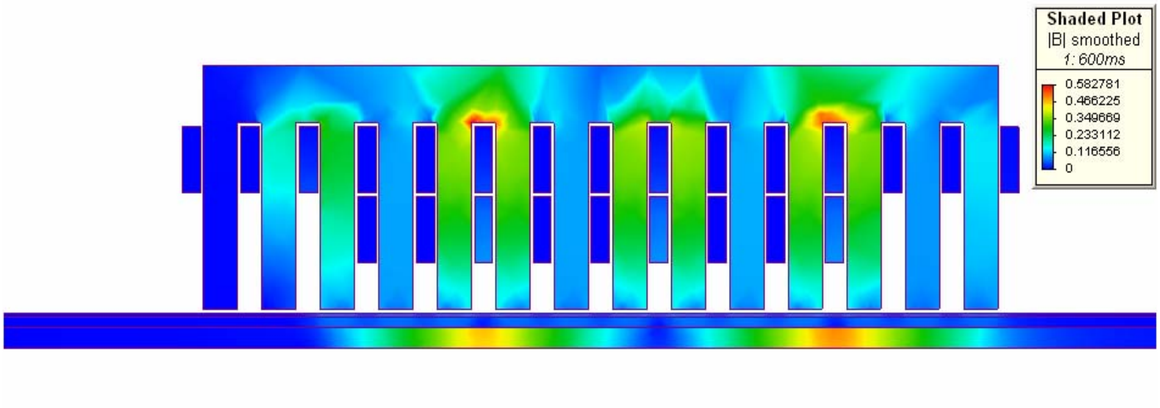

Figure 11 Flux Density Distribution when Phase c is Excited by a DC Current

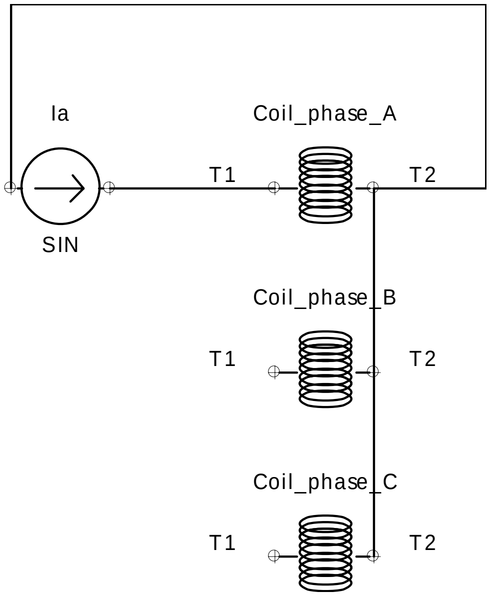

Figure 12 Excitation Circuit of Direct Method

Figure 13, 14, and 15 display the normal flux density in the middle of airgap when phases *a*, *b*, and *c* are excited by a dc current respectively. One can notice the waveform of phase *a* is the mirror image of the waveform of phase *c*. However, the waveform of phase *b* is antisymetric itself. This observation verifies that the structure of two open ends on the primary contributes to the magnetic asymmetry effects of LIM.

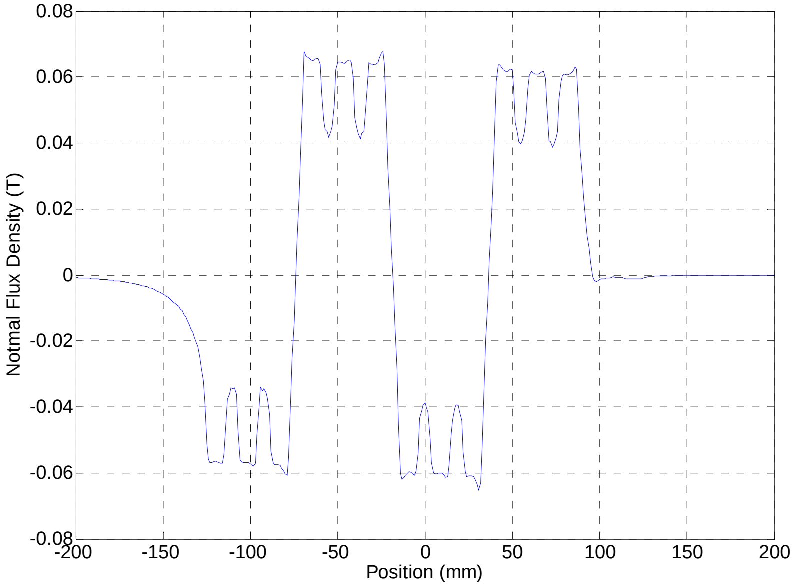

Figure 13 Normal Flux Density in the Middle of Airgap when Phase a is Excited by a DC Current

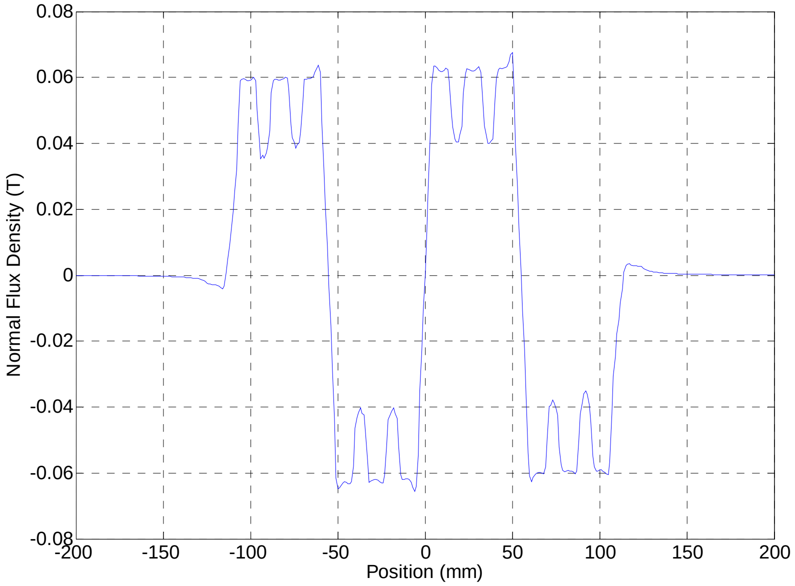

Figure 14 Normal Flux Density in the Middle of Airgap when Phase b is Excited by a DC Current

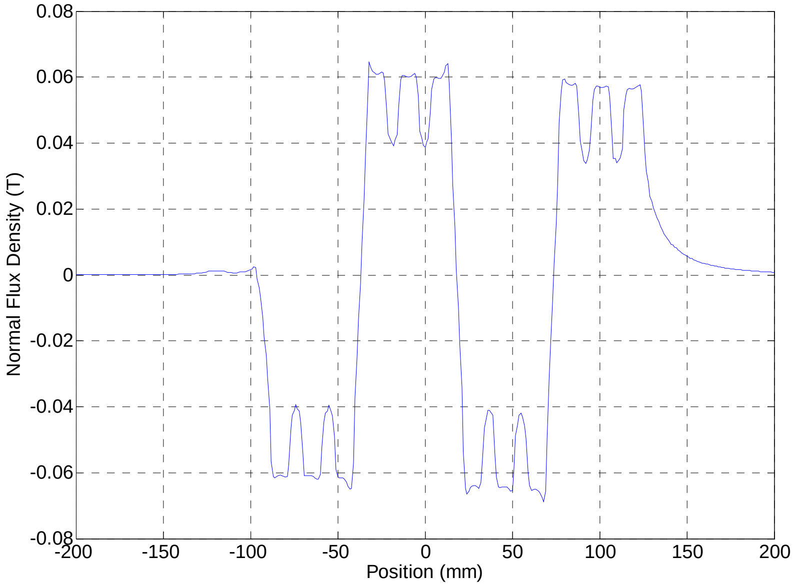

Figure 15 Normal Flux Density in the Middle of Airgap when Phase c is Excited by a DC Current

2.3.1 Experimental Verification of Magnetic Asymmetry Effects

Since the winding connection of primary is ‘Y’ connection without access to the neutral point, in order to implement experiments, the circuit shown in figure 16 (indirect method) has been used. In the indirect method, when one phase is excited by a dc current, the other two phases are connected in parallel to supply the return path for the first phase current. As a result, when phase *a* is excited and phase *b* and *c* are connected in parallel, this condition is defined as A-BC. Based on the above method, figure 17 shows the normal airgap flux density of three connections in FEA.

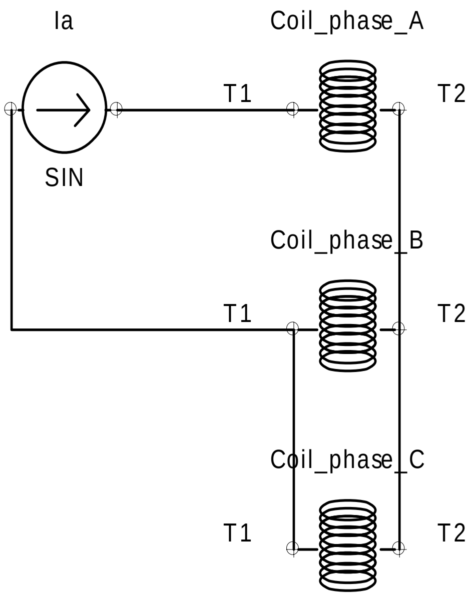

Figure 16 Indirect Excitation Method

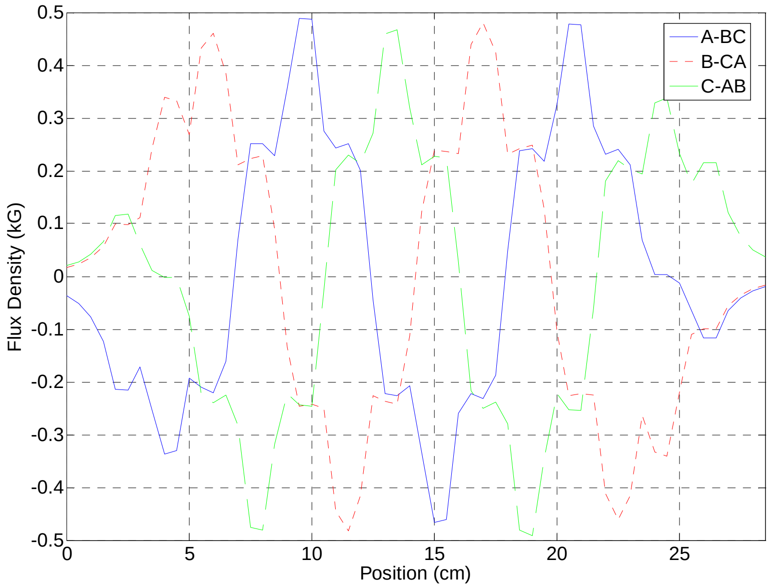

Figure 17 Normal Flux Density of Three Connections in FEA

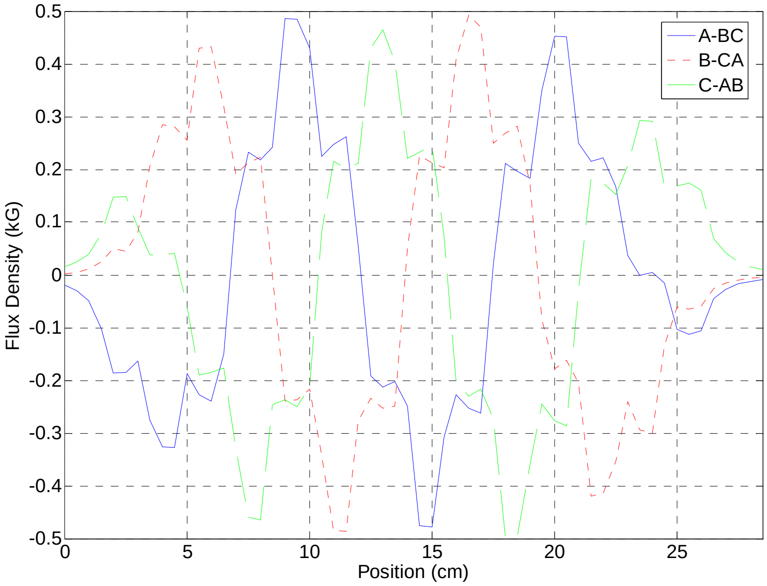

Figure 18 Normal Flux Density of Three Connections from Experimental Testbed

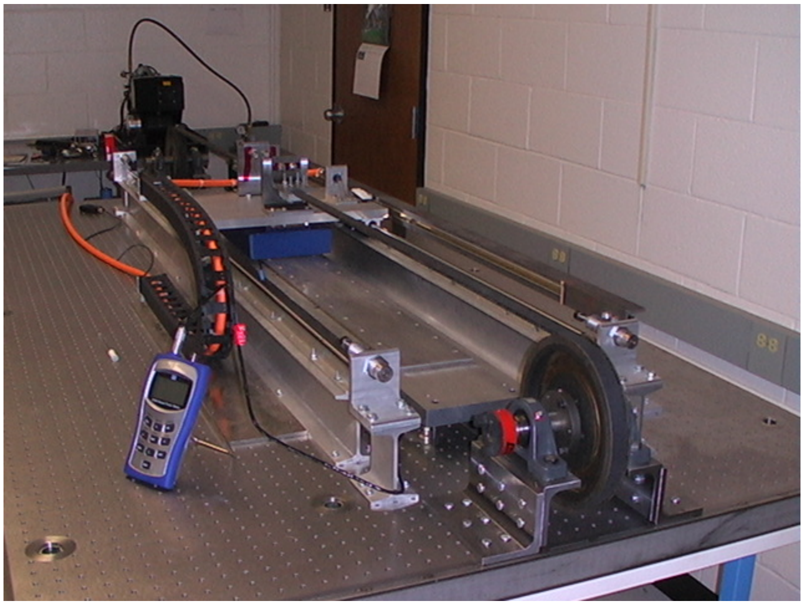

Figure 19 Prototype of LIM under Investigation

Figure 18 shows normal flux density of three connections of the experimental LIM testbed shown in figure 19. Figure 19 illustrates a single sided, three phase, 4 pole linear induction machine being investigated in this dissertation. In figure 19, the blue part in the middle of railway is primary, and beneath that is the aluminum sheet backed with iron core. Detailed information is given in APPENDIX A. Comparing figure 18 with figure 17, one can observe a close match between the two figures. In addition, it is shown that the waveform of excitation connection A-BC is mirror image to that of excitation connection C-AB. However, the waveform of excitation caused by B-CA connection is antisymetric itself. These observations are similar with the results from the direct method. Therefore, different relative positions of *a*, *b*, and *c* phases in primary result in the magnetic asymmetry effects.

From [28], for conventional rotary induction machines, the following equation holds:

$$MMF_s = K\cos(\omega_e t - \phi_s) \tag{1}$$

However, for LIM, due to the asymmetry between contributions of the primary phases, the above equation will not hold any more, even though a set of three phase, balanced, sinusoidal current sources are supplied. Figures 20-22 represent the flux linkage of each phase under three phase balanced current excitation. One can notice phase *a* and *c* have almost same magnitudes (about 0.27 Wb). However, phase *b* exhibits a flux linkage of magnitude bigger than 0.3 Wb. The difference of the flux linkage values is beyond 10%. Therefore, the flux linkage is not equally distributed among three phases. In fact, the resultant *MMF* will impact the force characteristic of the machine and will hinder the application of conventional indirect field oriented control of this family of machines.

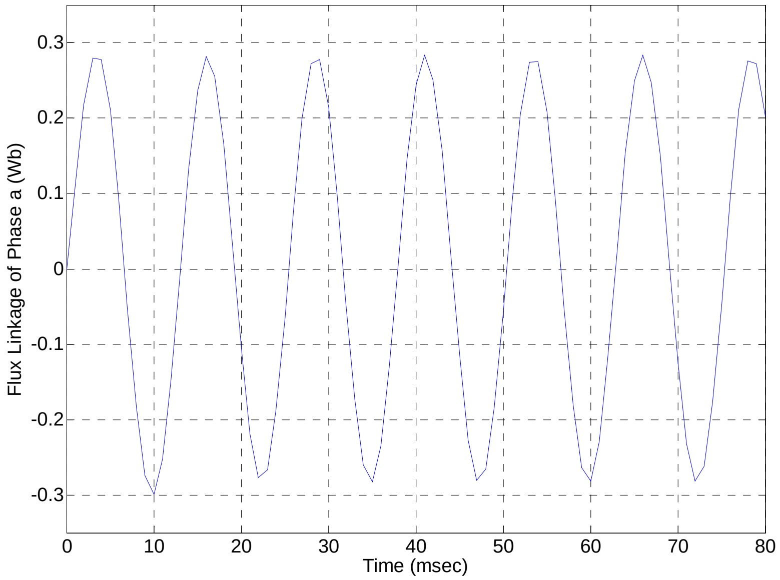

Figure 20 Flux Linkage of Phase a under a Set of Three Phase Balanced Sinusoidal Current Sources Excitation

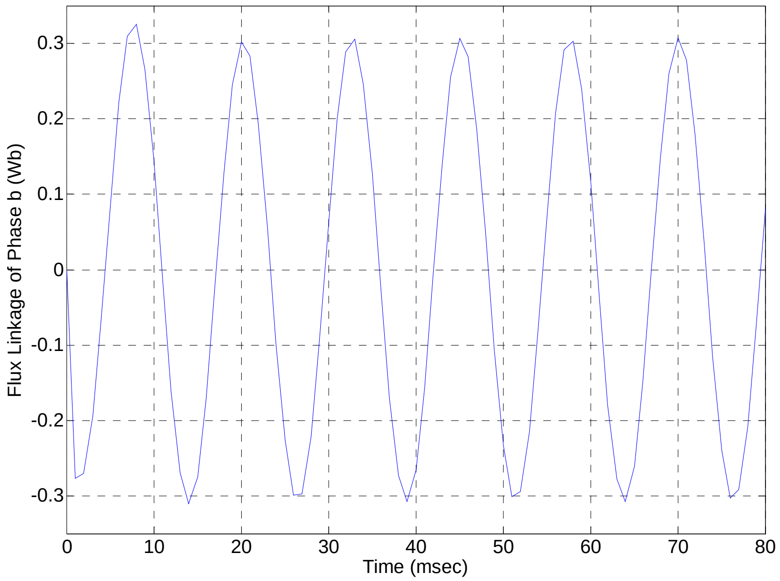

Figure 21 Flux Linkage of Phase b under a Set of Three Phase Balanced Sinusoidal Current Sources Excitation

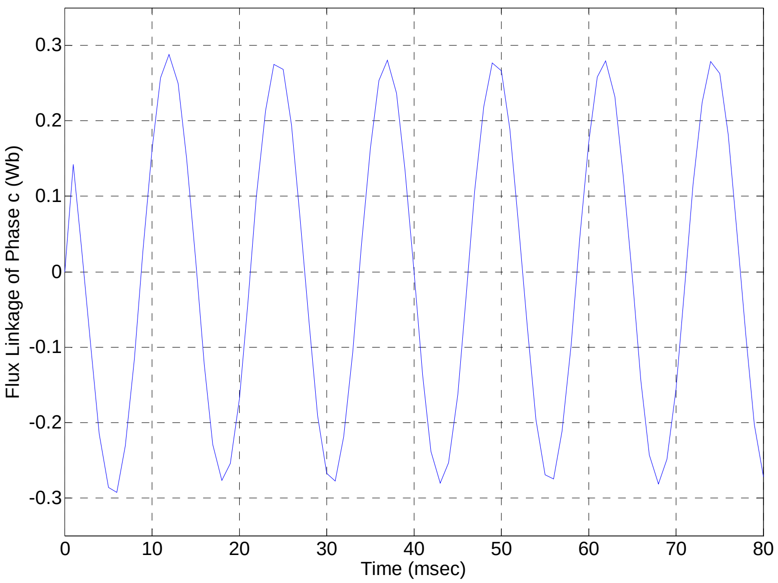

Figure 22 Flux Linkage of Phase c under a Set of Three Phase Balanced Sinusoidal Current Sources Excitation

2.3.2 Magnetic Asymmetry Effects on Force Characteristics of LIM

Figure 23 represents the variations of average thrust and normal force with respect to primary excitation frequency, where the power supply is a set of three phase, balanced current sources with an amplitude of 2 A. The linear speed is kept at 5 m/sec. As can be seen, in figure 23 the maximum thrusts during motoring and generating modes exhibit tangible differences. In addition, based on [20], from synchronous frequency to positive infinity, the linear induction machine operates as a motor; from 0 Hz to synchronous frequency, LIM works as a generator; and from negative infinity to 0 Hz, LIM operates under electromagnetic braking (System has electrical and mechanical inputs at the same time).

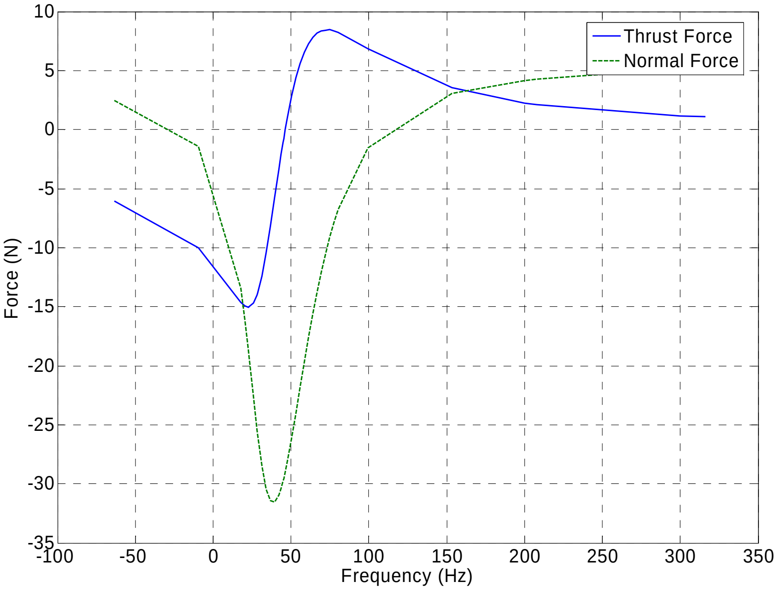

Figure 23 Average Force Variations with Respect to Frequency at Linear Speed of 5 m/sec

2.3.3 Magnetic Asymmetry Effects on IFOC of LIM

Due to the existence of trailing eddy current effects and magnetic asymmetry effects, the conventional indirect field oriented control may not supply its expected functionality as for rotary induction machines. Equation (2) and (3) govern the control strategy of indirect field oriented control. Figure 24 represents the block diagram of IFOC.

$$\omega_e = \frac{P}{2}\omega_r + \frac{1}{\tau_r}\frac{i_{qs}}{i_{ds}} \tag{2}$$

$$I_{rms} = \sqrt{\left(i_{qs}\right)^2 + \left(i_{ds}\right)^2} \tag{3}$$

where ω_e is the excitation frequency, P is No. of poles, ω_r is the equivalent angular speed of primary transformed from the corresponding linear speed v, τ_r is the secondary time constant, i_{qs} and i_{ds} are the commanded quadrature axis (q axis) current and direct axis (d axis) current respectively, and I_{rms} is the RMS value of phase current. Detailed discussion of indirect field oriented control will be conducted in chapter 4.

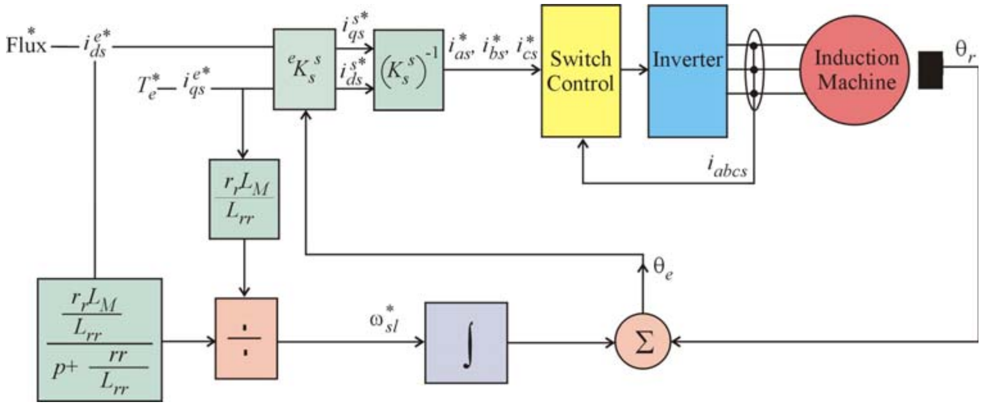

Figure 24 Block Diagram of IFOC Functionality

Figure 25 and 26 show the force variations with respect to I_q when I_d is fixed at 1 A under both motoring and generating conditions using indirect field oriented control. It can be observed that both thrust and normal force have significant asymmetry performance under motoring and generating conditions when indirect field oriented control is utilized. In figure 25, a change in sign of I_q represents switching between motoring and generating modes of operation. Negative sign of figure 23 and 26 mean that the normal force between primary and secondary is attractive.

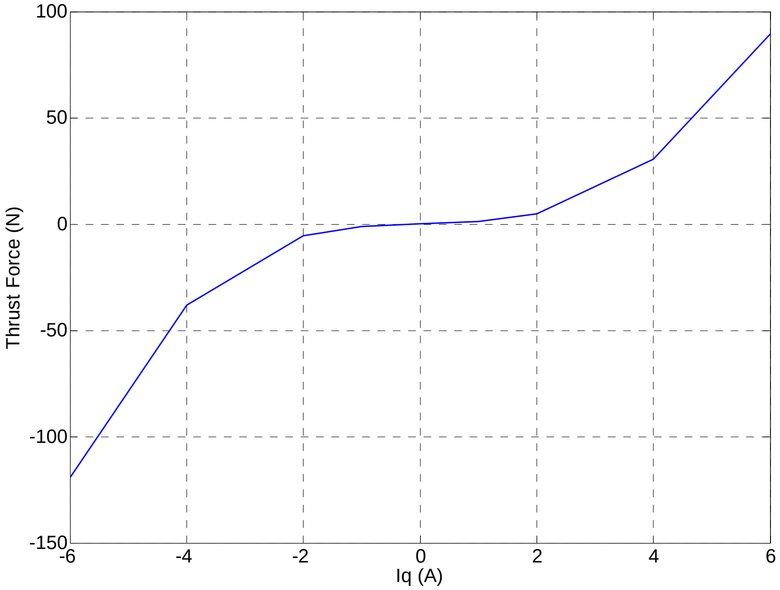

Figure 25 Average Thrust Variation with Respect to Iq when Id is Fixed at 1 A

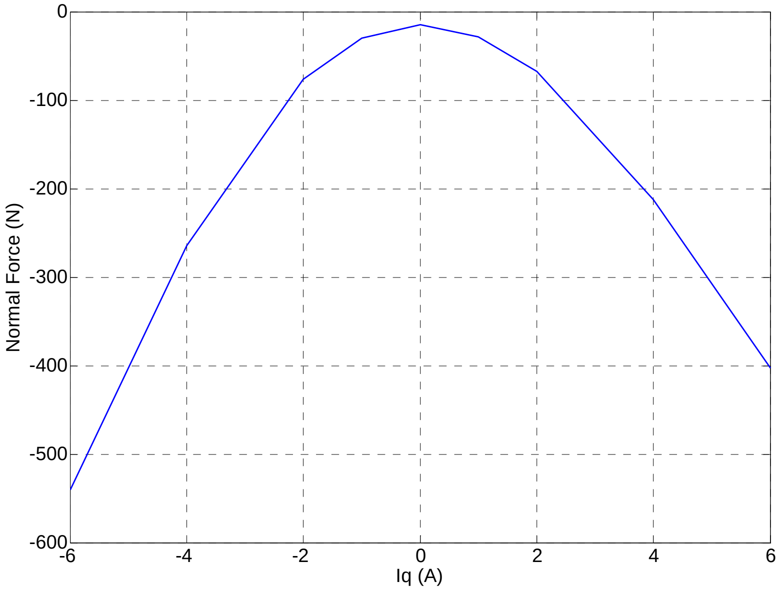

Figure 26 Average Normal Force Variation with Respect to Iq when Id is Fixed at 1 A

2.3.4 Investigation of Magnetic Asymmetry Effects on IFOC of LIM from a Magnetic Perspective

Figure 27 illustrates the peak magnitude of flux density in the primary with respect to I_q, when I_d is fixed at 1 A. Figure 28 is the similar characteristic with respect to I_d, when I_q is fixed at 1 A. From both curves, one can notice that there is a difference between motoring and generating conditions in figure 27. However, curves representing motoring and generating conditions in figure 28 match reasonably. Figure 29 illustrates the peak magnitude of flux density in the back iron of the secondary with respect to I_q, when I_d is fixed at 1 A. Figure 30 is the similar characteristic with respect to I_d, when I_q is fixed at 1 A. Again, there is a difference between motoring and generating conditions in figure 29. Curves of both motoring and generating conditions in figure 30 match well. The above observations indicate that the effect of I_q is not symmetric between motoring and generating conditions. However, I_d illustrates a symmetric influence during motoring and generating conditions. These observations require modification in the conventional indirect field oriented control scheme.

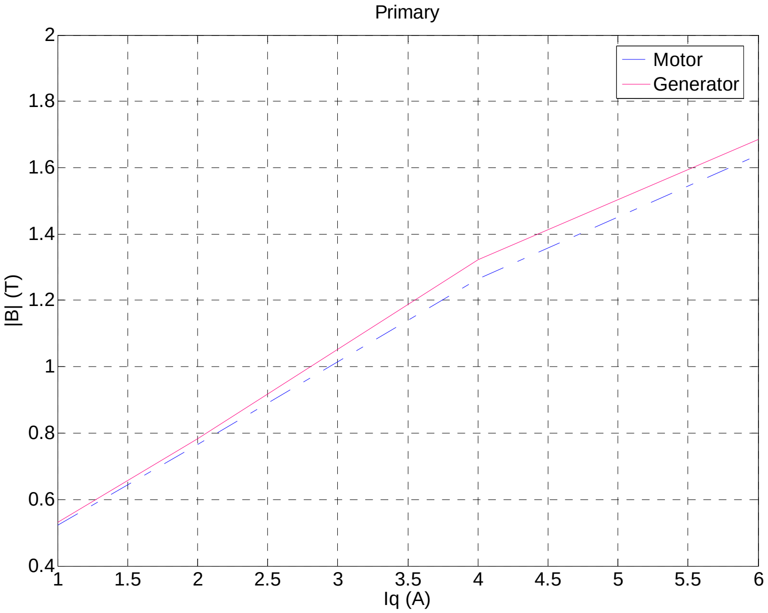

Figure 27 Magnetization Curve of Primary with Respect to Iq

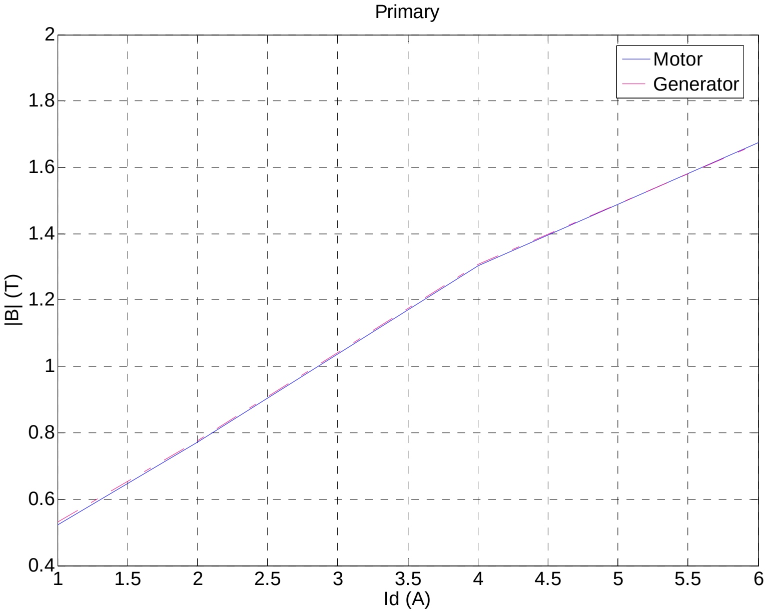

Figure 28 Magnetization Curve of Primary with Respect to Id

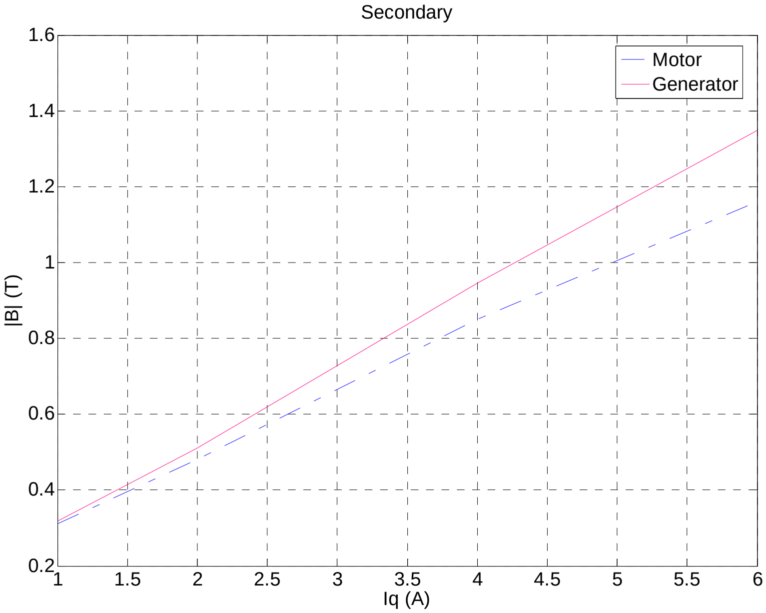

Figure 29 Magnetization Curve of Secondary with Respect to Iq

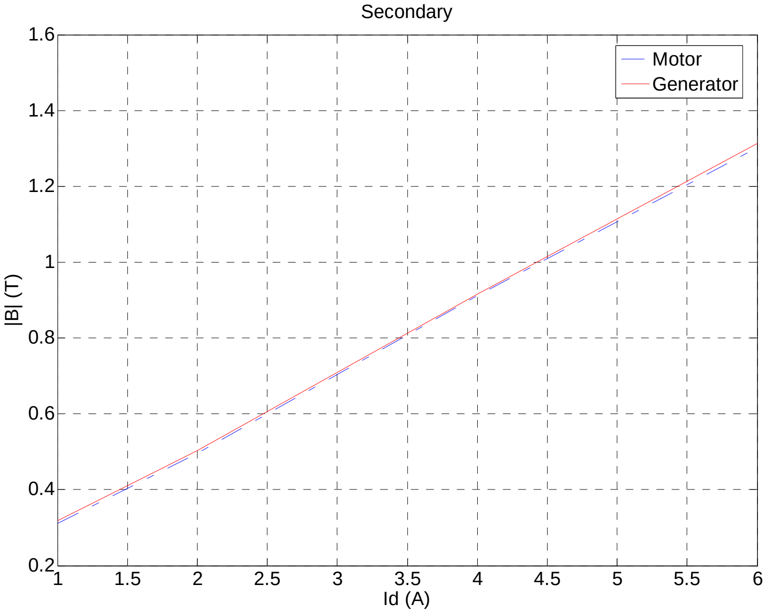

Figure 30 Magnetization Curve of Secondary with Respect to Id

2.4 Airgap Length Effect

The effect of airgap length on the force characteristics of LIM at low linear speeds has been explored in [1]. Since the force characteristics under high speeds are more important in propulsion applications, it is necessary to topologies the airgap length effects for the full speed range.

When linear speed is 1 m/sec (low speed range), and excitation frequency is 36.13 Hz (motoring), the airgap length is varied from 1.5 mm, to 2.5 mm, 3.5 mm, and 4.5 mm in sequence. Figure 31 displays the thrust and normal force variations with airgap length. The excitation is a set of three phase balanced current sources with amplitude of 2 A. When excitation frequency changes to 18.16 Hz (electromagnetic braking), figure 32 represents the force variations with respect to airgap length. From figure 31 and 32, one can observe that both thrust and normal force monotonically decrease with airgap length. This phenomenon matches with [1]. Furthermore, linear speed is increased to 10 m/sec to represent the high speed range. Figure 33 and 34 represent the force variations with respect to airgap length under motoring (116.98 Hz) and generating (57.26 Hz) conditions respectively. From figure 33, one can notice that the thrust does not change monotonically any more. The thrust reaches the peak value when airgap length is 2.5 mm, and then drops. When machine works under generating condition (figure 34), thrust and normal force monotonically decrease with airgap length. However, there is a discontinuity in the normal force changing trend. When linear speed is 15 m/sec, the force characteristics with respect to airgap length under motoring and generating conditions are shown in figure 35 and 36 respectively. Figure

35 shows that the thrust has a maximum value at 3.5 mm airgap length. Compared with value of figure 33, there is a trend that when linear speed increases the airgap length for the maximum thrust also increases. In figure 36, the normal force has the maximum value when airgap length is 2.5 mm. This change is different from that illustrated in figures 32 and 34.

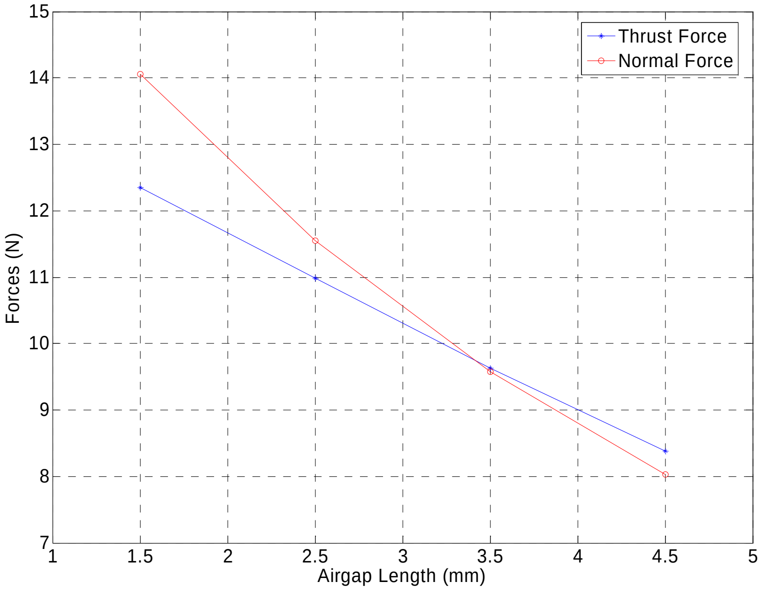

Figure 31 Force Variations with Respect to Airgap Length under Motoring Condition (1 m/sec)

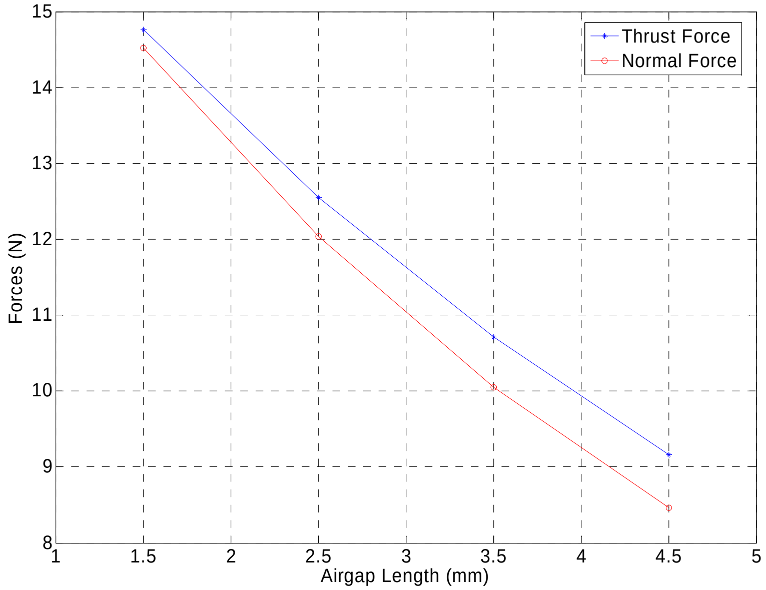

Figure 32 Force Variations with Respect to Airgap Length under Electromagnetic Braking Condition (1 m/sec)

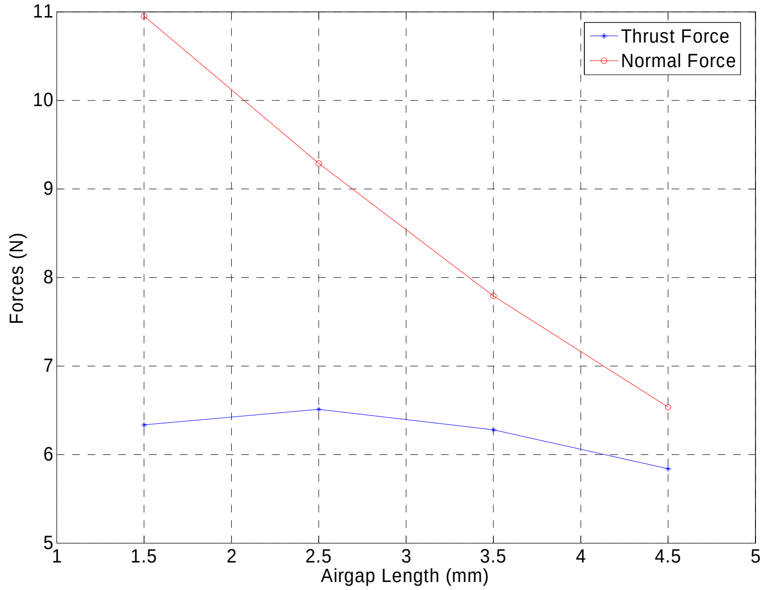

Figure 33 Force Variations with Respect to Airgap Length under Motoring Condition (10 m/sec)

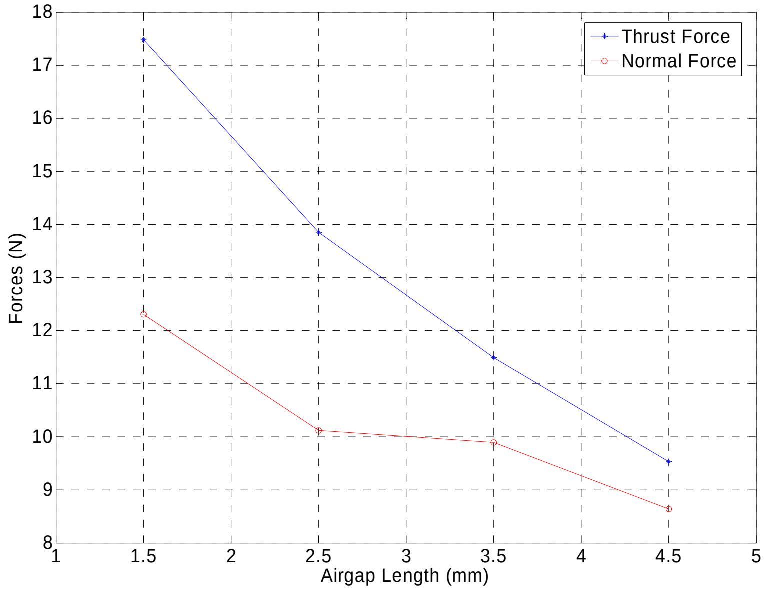

Figure 34 Force Variations with Respect to Airgap Length under Generating Condition (10 m/sec)

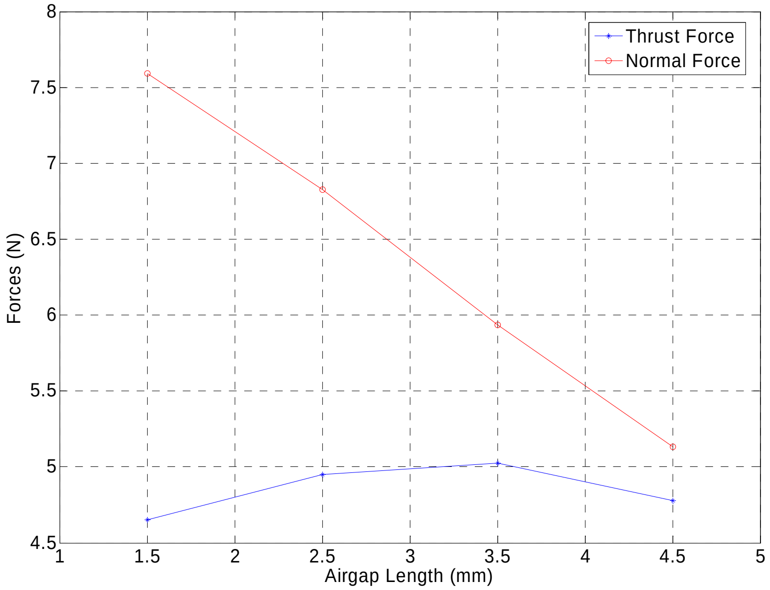

Figure 35 Force Variations with Respect to Airgap Length under Motoring Condition (15 m/sec)

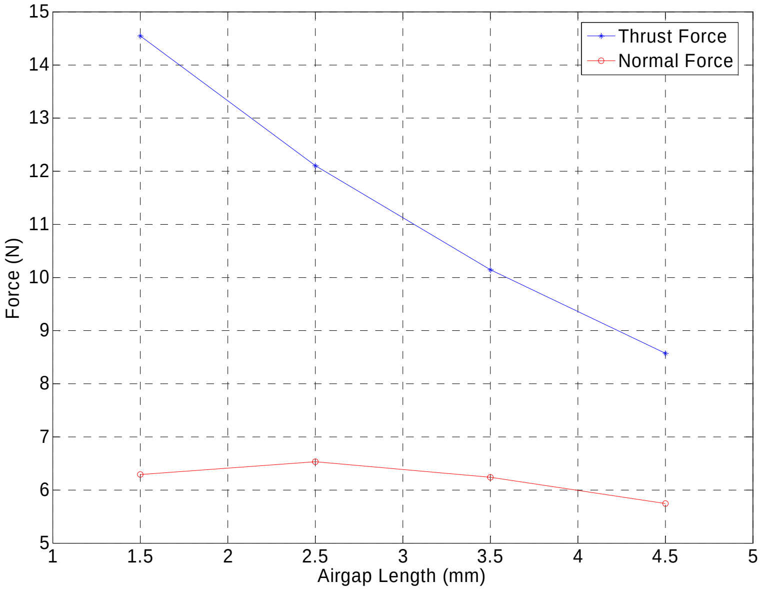

Figure 36 Force Variations with Respect to Airgap Length under Generating Condition (15 m/sec)

2.5 Secondary Electric Conductivity’s Effect

In most applications, the resistance of LIM secondary aluminum plate is subject to the ambient temperature change and heating effect caused by eddy current. This effect is governed by the following equation:

$$R_r = \frac{234.5 + t_r}{234.5 + t_n} \times R_n \tag{4}$$

R_n is the nominal value of secondary resistance, R_r is the real value of resistance, t_n is the nominal temperature, and t_r is the real temperature.

The varying secondary resistance will also affect the secondary electric conductivity. It is necessary to investigate how secondary electric conductivity affects the force characteristics of LIM. Figure 37 and 38 represent the thrust and normal force variations with respect to secondary electric conductivity at 1 m/sec and 15 m/sec respectively. One can notice the increment of secondary electric conductivity causes significant drop of normal force. However, the variation of electric conductivity does not affect thrust very much. These observations mean that the variation of secondary electric conductivity can cause significant normal force ripples.

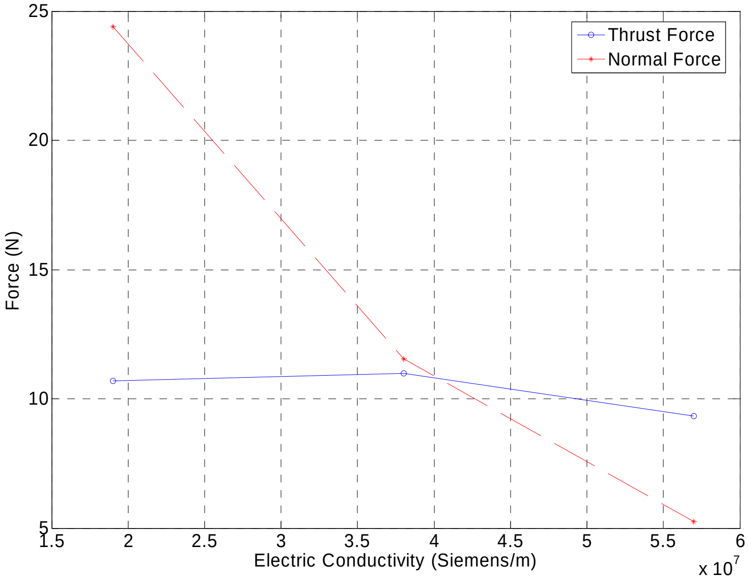

Figure 37 Force Variation with Secondary Electric Conductivity at Linear Speed 1 m/sec

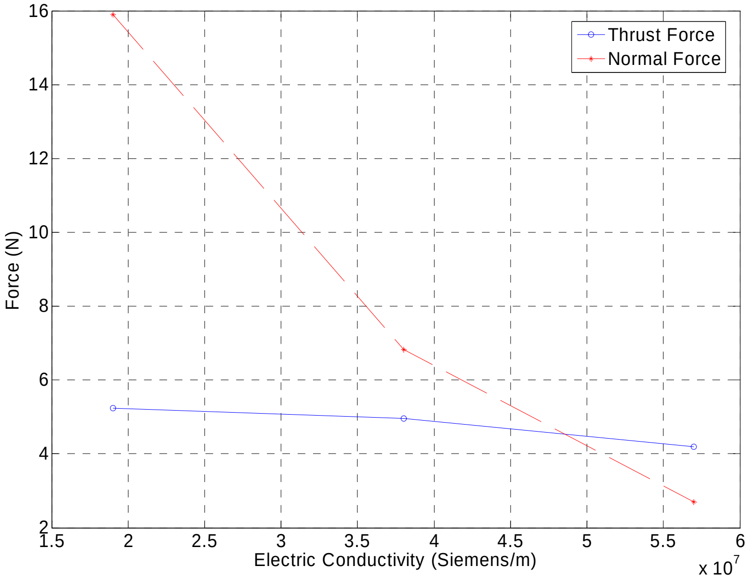

Figure 38 Force Variation with Secondary Electric Conductivity at Linear Speed 15 m/sec

2.6 Back EMF Characteristics

Figure 39 and 40 are the back EMF amplitude variations with respect to frequency when linear speed is 1 m/sec and 5 m/sec respectively. For LIM, the thrust can be related to the electrical input by the following equations:

$$F_t = \frac{P_{electrical}}{V_{linear}} \tag{5}$$

$$P_{electrical} = E_a I_a \cos(\phi_a) + E_b I_b \cos(\phi_b) + E_c I_c \cos(\phi_c) \tag{6}$$

where F_t is the thrust force, $P_{electrical}$ is the total electrical power, V_{linear} is the linear velocity of LIM, E_n (n=a, b, or c) is the magnitude of back EMF, I_n is the magnitude of phase current, and ϕ_n is the phase shift between back EMF and phase current. From figure 39 and 40, it can be observed that when excitation is a set of three phase balanced dc current sources (0 Hz), the amplitude of back EMF is very close to 0. In addition, when increase excitation frequency to positive or negative infinity, the amplitude of back EMF increases monotonically. This fact will cause a high stress on power electronic components when excitation frequency is very high, which may result in control failure of LIM drive. Based on the data from figure 39 and 40, and equation (5) and (6), one can plot the phase shift between the back EMF and phase current shown in figure 41 and 42. Figure 41 has hyperbolic waveforms in first and second quadrants. Figure 42 has the minimum phase shift at 66.62 Hz, and saturates to 90 degrees in the positive infinity frequency.

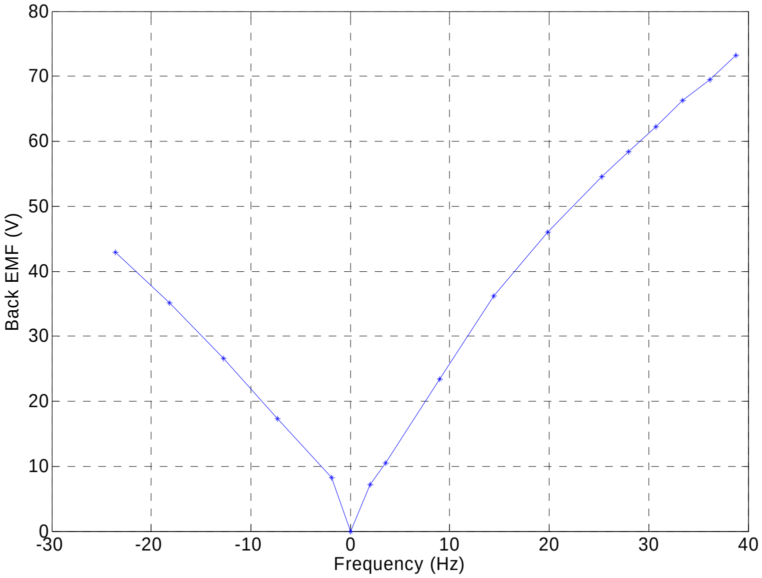

Figure 39 Back EMF Amplitude Variation with Frequency at 1 m/sec

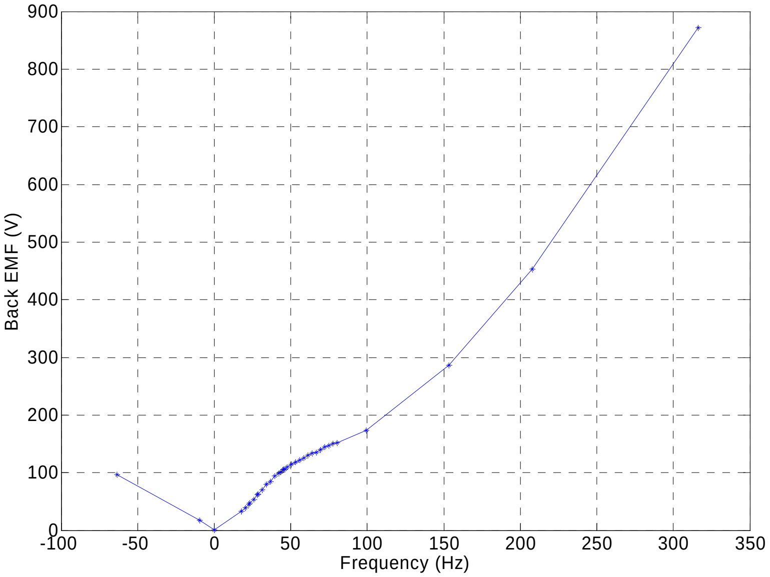

Figure 40 Back EMF Amplitude Variation with Frequency at 5 m/sec

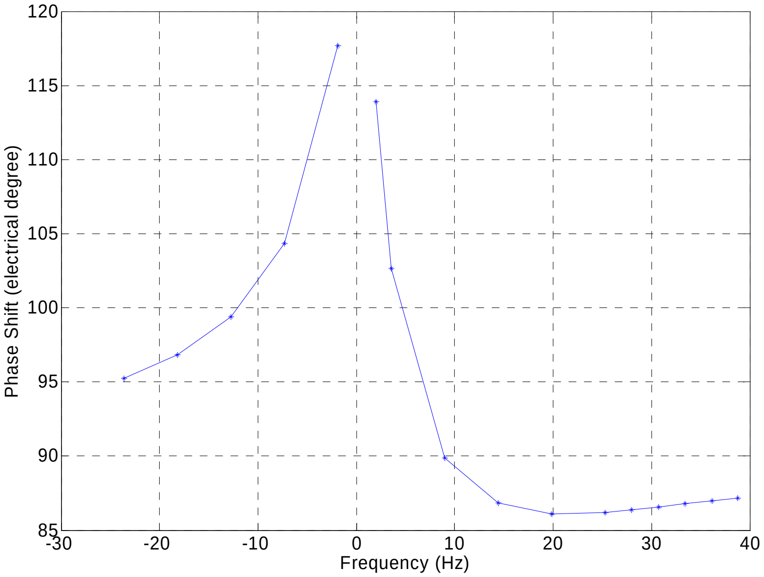

Figure 41 Phase Shift between Back EMF and Phase Current at 1 m/sec

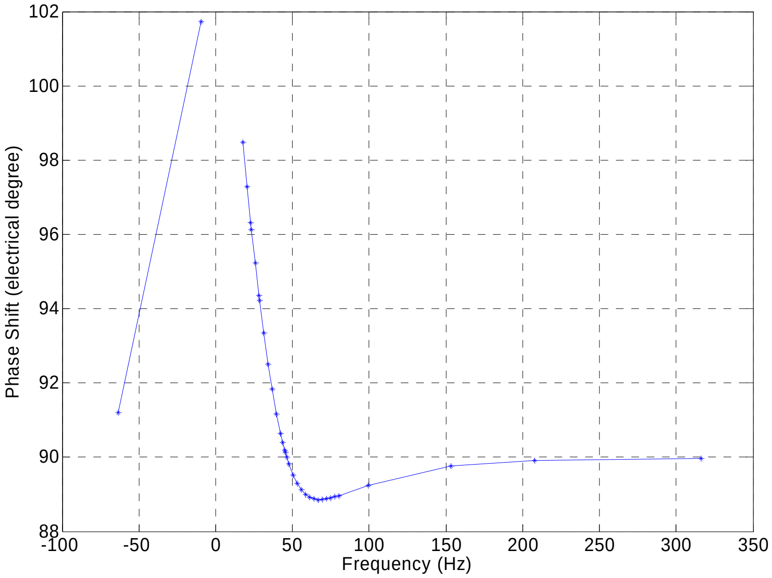

Figure 42 Phase Shift between Back EMF and Phase Current at 5 m/sec

CHAPTER 3

FIELD RECONSTRUCTION METHOD OF LINEAR INDUCTION MACHINES

In the last chapter, electromagnetic behavior of LIM has been investigated based on FEA, and verified by experimental results. FEA is well known and widely used as a tool for numerical-based analysis of electric machines. However, the computational effort required to complete a finite element evaluation is significant. Therefore, a so-called field reconstruction method (FRM) for LIM has been developed. FRM only requires few number of FEA evaluations to reconstruct the fields in the middle of airgap for any set of given excitation and positions. Based on the knowledge of fields in the middle of airgap and Maxwell Stress Tensor (MST) method [29] and [30], one can predict the forces acting on the primary.

3.1 Background

All force calculations throughout this chapter are based on MST method. Using MST, the tangential and normal force densities in the middle of airgap can be expressed as follows:

$$f_x = \frac{1}{\mu_o} B_x B_y \tag{7}$$

$$f_y = \frac{1}{2\mu_o} (B_y^2 - B_x^2) \tag{8}$$

where B_x and B_y are the tangential and normal components of the flux densities in the middle of airgap of the machine and μ_o is the permeability of the air; f_x and f_y are the tangential and normal force densities in the airgap. The positive directions of normal and tangential components are defined in figure 43.

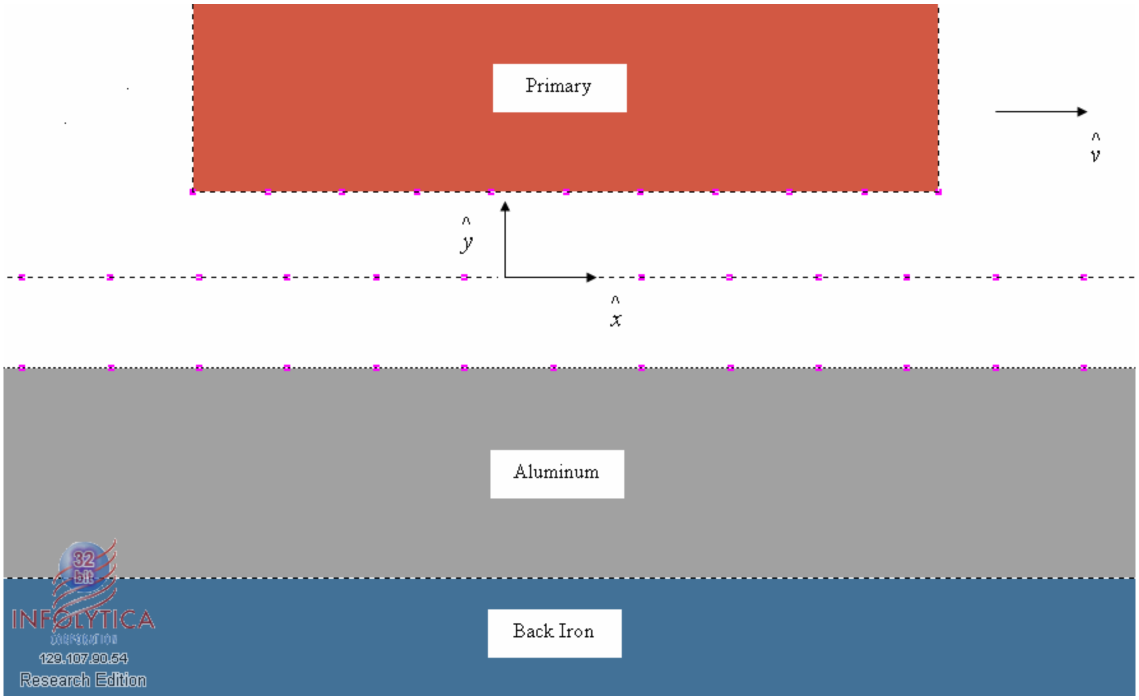

Figure 43 Positive Directions of Normal and Tangential Components

Therefore, the thrust and normal force can be expressed by

$$F_t = z\int_l f_x dl \tag{9}$$

$$F_n = z\int_l f_y dl \tag{10}$$

where z is the stack length of LIM, F_n is the normal force.

The following assumptions have been made for the investigation of FRM. The flux density in the axial direction is zero, which means no end effect is included. The machine is not saturated, such that the superposition can be applicable. Hysteresis and eddy currents in the primary and secondary back iron are neglected. The operating temperature is assumed to be constant. In another word, the heating effect to machine parameters can be neglected. Furthermore, the primary teeth are assumed to be rigid.

3.2 Basis Function Identification

Based on the assumption of no saturation, the normal and tangential components of flux density in the middle of airgap can be expressed by the sum of primary and secondary quantities.

$$B_x = B_{xs} + B_{xr} \tag{11}$$

$$B_y = B_{ys} + B_{yr} \tag{12}$$

where B_{xs} and B_{xr} are tangential flux densities of primary and secondary respectively, and B_{ys} and B_{yr} are normal flux densities of primary and secondary respectively. These four quantities are also defined as ‘Basis Function’.

3.2.1 Primary Basis Function Derivation

At the first step, a static FEA evaluation is used to derive the primary basis function of phase *a*. In the FEA program, primary is fixed in the middle of the secondary railway to eliminate the railway asymmetry effect on the primary basis function. In another word, the length of secondary railway is assumed to be infinity. In addition, phase *a* current i_a is set with 1 A dc current, and phases *b* and *c* are open. The normal and tangential flux densities are calculated and stored as basis functions B_{xsa} and B_{ysa} respectively. In order to store the basis functions, the infinite railway of secondary is truncated into an effective and finite length. Furthermore, the effective airgap is discretized into n equally distributed points. Hence, B_{xsa} and B_{ysa} are represented as two n by 1 vectors in computer. Because of the magnetic asymmetry effects of primary, in order to calculate the basis functions of phases *b* and *c*, the same procedure for phase *a* has to be repeated in phase *b* and *c* respectively. Figure 44 and 45 illustrate the basis functions of normal and tangential flux densities respectively.

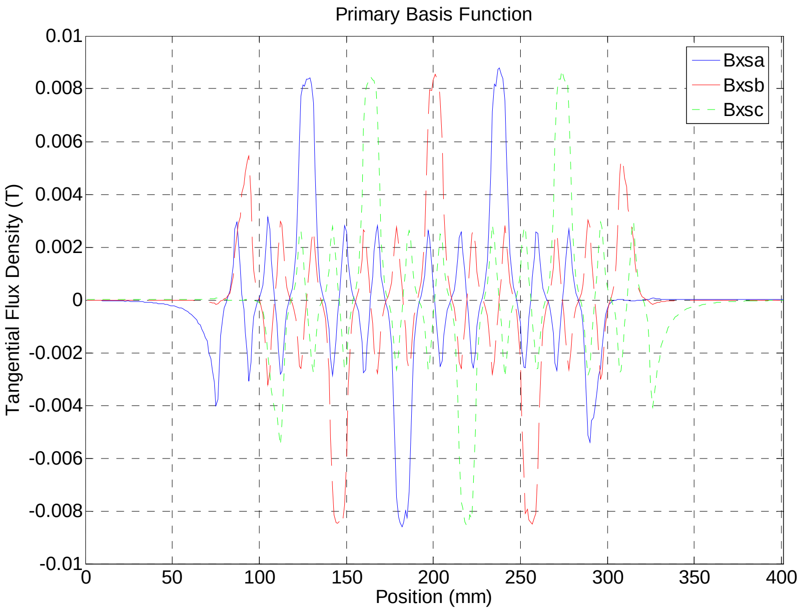

Figure 44 Tangential Basis Functions of Three Phases

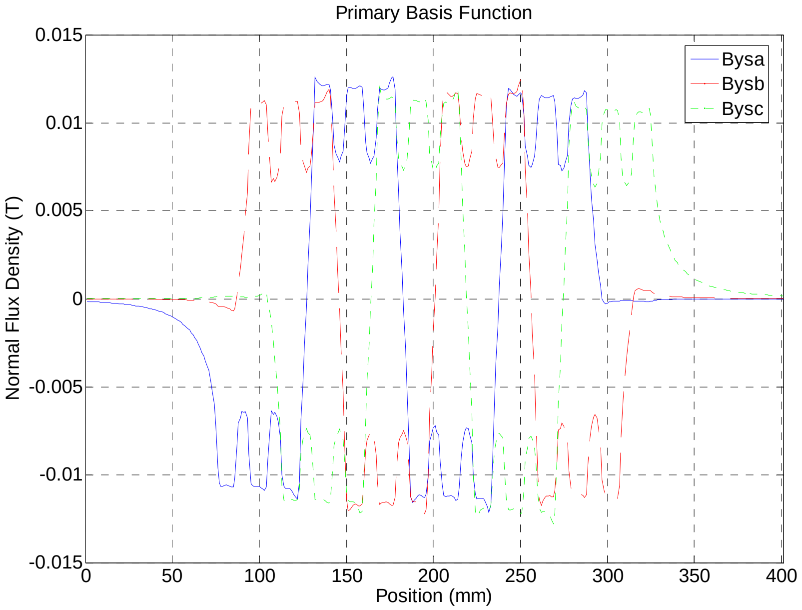

Figure 45 Normal Basis Functions of Three Phases

Using these basis functions, the flux density contributed by primary with arbitrary three phase currents can be expressed as follows:

$$B_{xs}(l) = i_a B_{xsa}(l) + i_b B_{xsb}(l) + i_c B_{xsc}(l) \tag{13}$$

$$B_{ys}(l) = i_a B_{ysa}(l) + i_b B_{ysb}(l) + i_c B_{ysc}(l) \tag{14}$$

where l is the position information on the effective airgap.

3.2.2 Secondary Basis Function Derivation

Unlike B_{xs} and B_{ys}, B_{xr} and B_{yr} are not only determined by the instantaneous primary current, they are also subject to the change of the primary current. In fact, B_{xr} and B_{yr} are generated by secondary eddy current, which results from primary current and primary motion. However, in reality, the electromagnetic forces are only determined by the slip frequency ω_{slip}, which can be expressed as

$$\omega_{slip} = \omega_e - \frac{P}{2}\omega_r \tag{15}$$

Therefore, ω_{slip} is the combined result of electrical and mechanical systems. In the procedure of FR for LIM, for a given excitation frequency and linear speed, the electrical angular frequency corresponding to the linear speed is subtracted from the excitation frequency, and the result is the slip frequency. In order to identify secondary basis functions, the primary speed is set at $v = 0$. Using a transient FEA evaluation, an impulse current is used as phase *a* current input signal. The impulse input has a value of 1 A at t_0, and 0 elsewhere. A sequence of normal and tangential flux densities for $t \geq t_0$ is then recorded. Using previously established primary basis functions, the flux densities generated by secondary eddy current can be represented as follows

$$B_{xra} = B_{xim} - B_{xsa} \tag{16}$$

$$B_{yra} = B_{yim} - B_{ysa} \tag{17}$$

where B_{xim} and B_{yim} are the recorded values of flux densities due to the impulse current input, and B_{xra} and B_{yra} are secondary basis functions of phase *a*. Using the same procedure, secondary basis functions of phase *b* and *c* can also be identified. Furthermore, all secondary basis functions are in the format of matrices. The rows of the matrices represent the n points along the effective airgap; the columns of matrices describe the impulse response of these points in the time domain. Therefore, the normal and tangential flux densities due to secondary eddy current can be summarized as following two equations:

$$B_{xr}(l,t) = i_a(t) * B_{xra}(l,t) + i_b(t) * B_{xrb}(l,t) + i_c(t) * B_{xrc}(l,t) \tag{18}$$

$$B_{yr}(l,t) = i_a(t) * B_{yra}(l,t) + i_b(t) * B_{yrb}(l,t) + i_c(t) * B_{yrc}(l,t) \tag{19}$$

where ‘$*$’ denotes the operation of convolution.

The two step procedure of basis function identification is shown in figure 46.

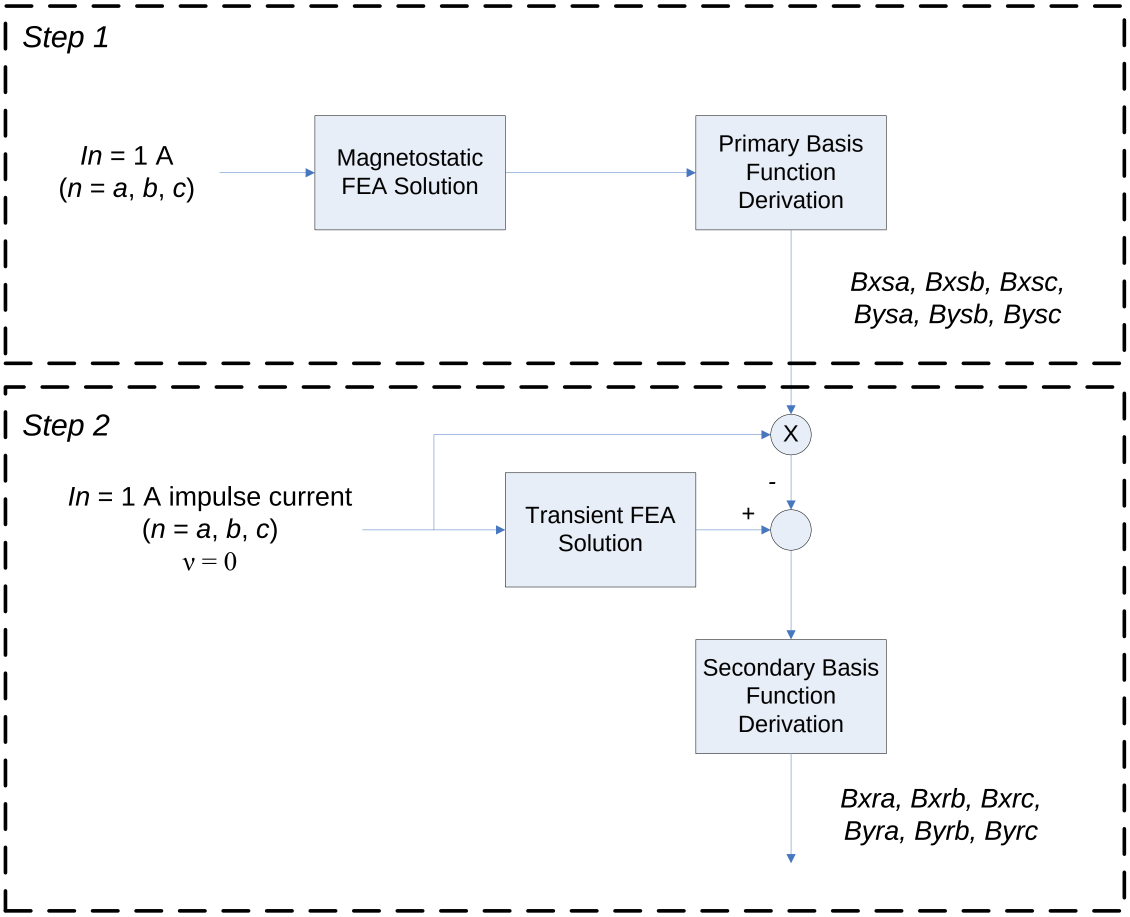

Figure 46 Two Step Procedure of Basis Function Identification

3.3 Field Reconstruction

Once all basis functions have been identified, the total tangential and normal flux densities B_x and B_y in the middle of airgap due to arbitrary primary excitation current can be obtained as:

$$\begin{aligned} B_x(l,t) &= i_a(t)B_{xsa}(l) + i_b(t)B_{xsb}(l) + i_c(t)B_{xsc}(l) \\ &+ i_a(t) * B_{xra}(l,t) + i_b(t) * B_{xrb}(l,t) + i_c(t) * B_{xrc}(l,t) \end{aligned} \tag{20}$$

$$\begin{aligned} B_y(l,t) &= i_a(t)B_{ysa}(l) + i_b(t)B_{ysb}(l) + i_c(t)B_{ysc}(l) \\ &+ i_a(t) * B_{yra}(l,t) + i_b(t) * B_{yrb}(l,t) + i_c(t) * B_{yrc}(l,t) \end{aligned} \tag{21}$$

Since the secondary basis functions are in the discrete time domain, the operation of convolution in equation (20) and (21) will be conducted in discrete time domain.

$$\begin{aligned} B_x(l,t_k) &= i_a(t_k)B_{xsa}(l) + i_b(t_k)B_{xsb}(l) + i_c(t_k)B_{xsc}(l) \\ &+ \sum_{m=1}^{k} i_a(t_m)B_{xra}(l,t_k - t_m) + \sum_{m=1}^{k} i_b(t_m)B_{xrb}(l,t_k - t_m) + \sum_{m=1}^{k} i_c(t_m)B_{xrc}(l,t_k - t_m) \end{aligned} \tag{22}$$

$$\begin{aligned} B_y(l,t_k) &= i_a(t_k)B_{ysa}(l) + i_b(t_k)B_{ysb}(l) + i_c(t_k)B_{ysc}(l) \\ &+ \sum_{m=1}^{k} i_a(t_m)B_{yra}(l,t_k - t_m) + \sum_{m=1}^{k} i_b(t_m)B_{yrb}(l,t_k - t_m) + \sum_{m=1}^{k} i_c(t_m)B_{yrc}(l,t_k - t_m) \end{aligned} \tag{23}$$

Finally, using MST the force densities and then electromagnetic forces can be computed. The procedure is shown in figure 47.

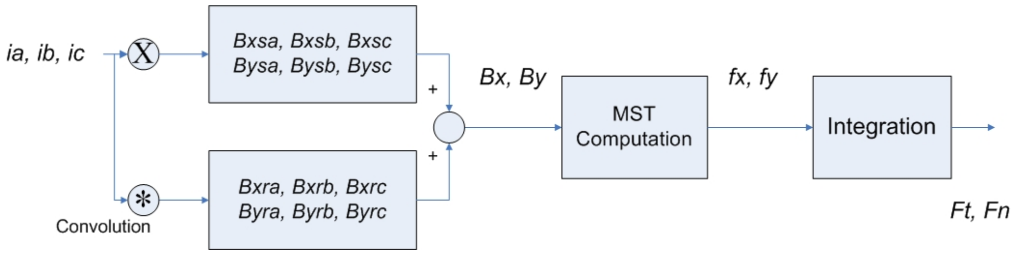

Figure 47 Field Reconstruction Procedure

3.4 Verification of Field Reconstruction

To verify the effectiveness of the proposed FR method, the constant speed operation is simulated. Constant speed operation is useful in evaluation of LIM steady state performance. In the following session, the comparison between direct FEA, slip frequency FEA, and FRM will be investigated. The direct FEA is the FEA simulation including the linear speed. Slip frequency FEA is the transient FEA program that uses the slip frequency in the excitation instead of real frequency, and does not have linear motion. FRM is the simulation conducted in Matlab/Simulink that utilizes the slip frequency excitation method to reconstruct fields of the LIM. Since the experimental test will be conducted at linear speed of 0.1 m/sec, the linear speed is also set to 0.1 m/sec in the constant speed operation for comparison. The electrical angular frequency corresponding to 0.1 m/sec is 1 Hz. Therefore when excitation frequency is 51 Hz, the slip frequency will be 50 Hz. At $t = 0$ sec, the commanded three phase current are activated. The flux densities results from both slip frequency FEA and FRM at $t = 0.1$ sec are shown in figure 48 and 49 respectively. One can notice there is no visual difference between slip frequency FEA and FRM. Figure 50 and 51 illustrate the normal flux density variations at the same position from FRM and experiment testbed. The output of the flux meter to oscilloscope is voltage signal. The amplitude of this voltage signal is 1.06 V, which is corresponding to about 0.05 T. One can notice the results from figure 50 and 51 match well.

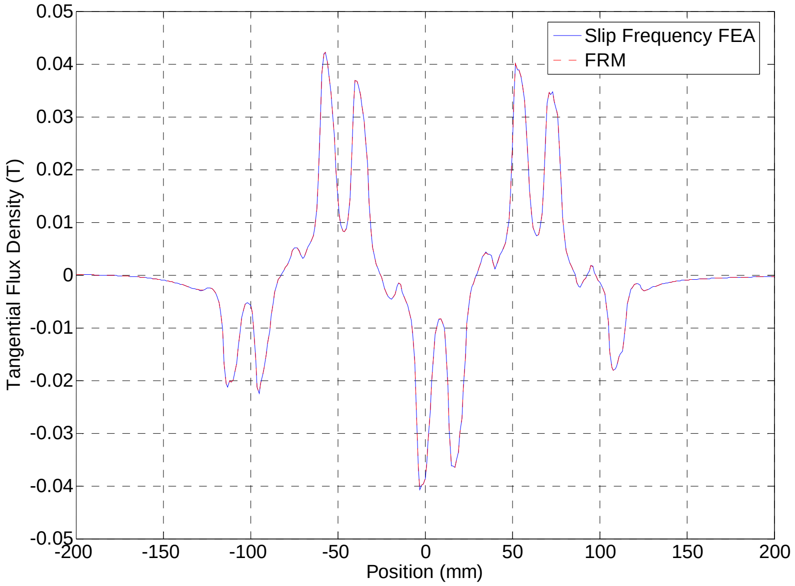

Figure 48 Tangential Flux Density

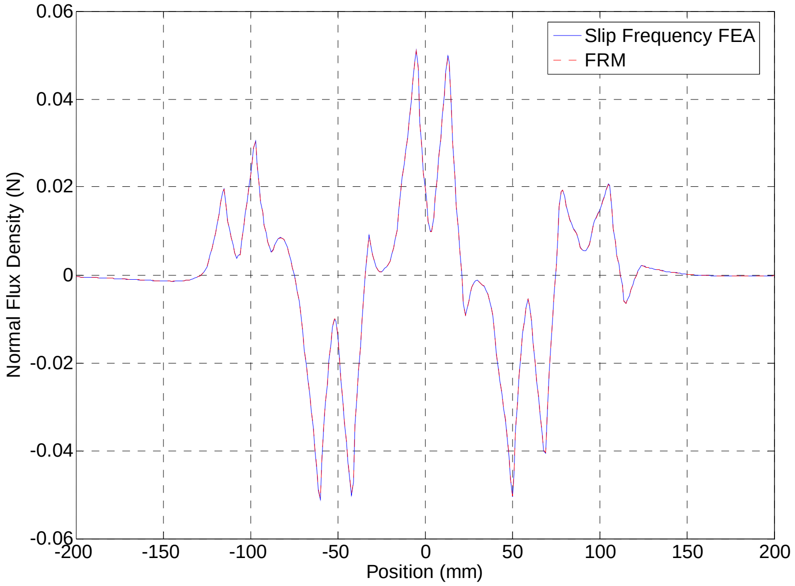

Figure 49 Normal Flux Density

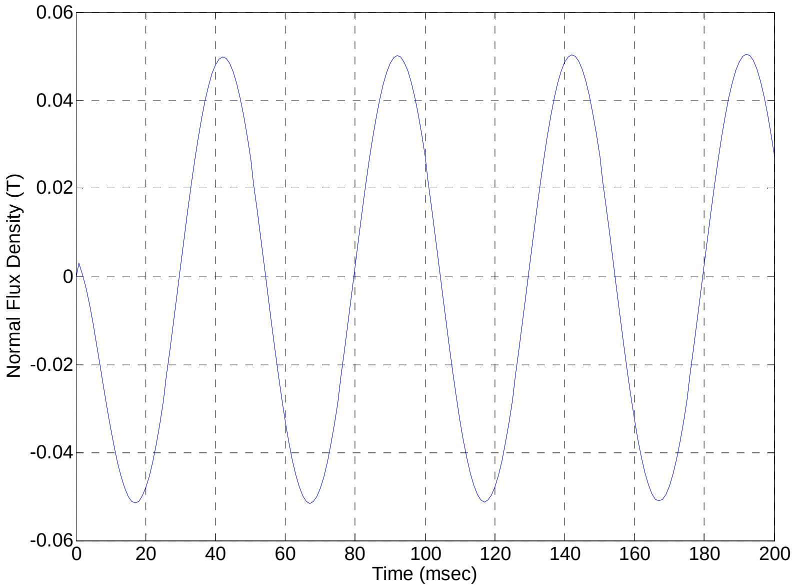

Figure 50 Normal Flux Density in the Middle of Airgap at One Particular Position Using FRM

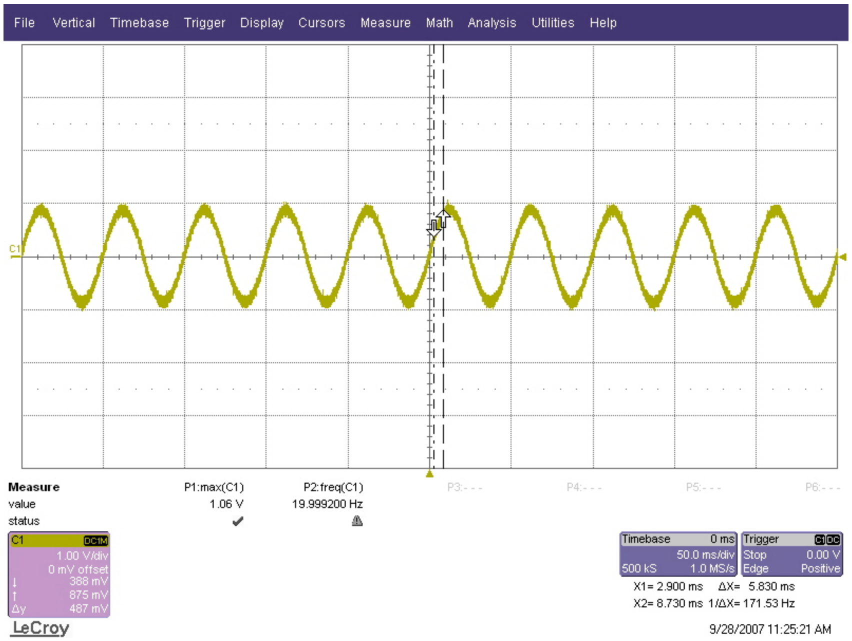

Measure	P1:max(C1)	P2:freq(C1)
value	1.06 V	19.999200 Hz
status	✓	⚠

C1 DC1M
1.00 V/div
0 mV offset
↓ 388 mV
↑ 875 mV
Δy 487 mV

Timebase 0 ms
50.0 ms/div
500 kS 1.0 MS/s

Trigger C1 DC
Stop 0.00 V
Edge Positive

X1= 2.900 ms ΔX= 5.830 ms
X2= 8.730 ms 1/ΔX= 171.53 Hz

9/28/2007 11:25:21 AM

Figure 51 Normal Flux Density in the Middle of Airgap at the Same Position with Figure 50 from Experiment (0.05 T/Div)

Using MST, the thrust and normal force variations with time are illustrated in figure 52 and 53 respectively. One can notice in steady state there are small values of dc error between these three methods. The reason of the dc error between direct FEA and slip frequency FEA is that the slip frequency FEA has no motion; therefore, there is no trailing eddy current effect in the slip frequency FEA. The dc error between slip frequency FEA and FRM is caused by truncating the infinite railway into a finite effective railway with airgap and using finite discrete time domain convolution. In addition, one can notice due to the existence of the trailing eddy currents, the thrust value from direct FEA is less than the value from FRM. In another word, trailing eddy current can degrade the force performance of LIM.

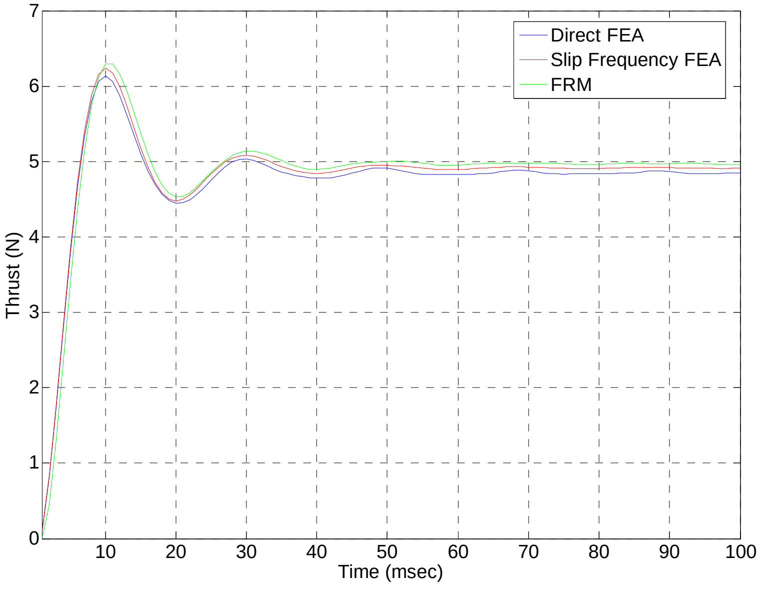

Figure 52 Thrust Variations of Three Methods

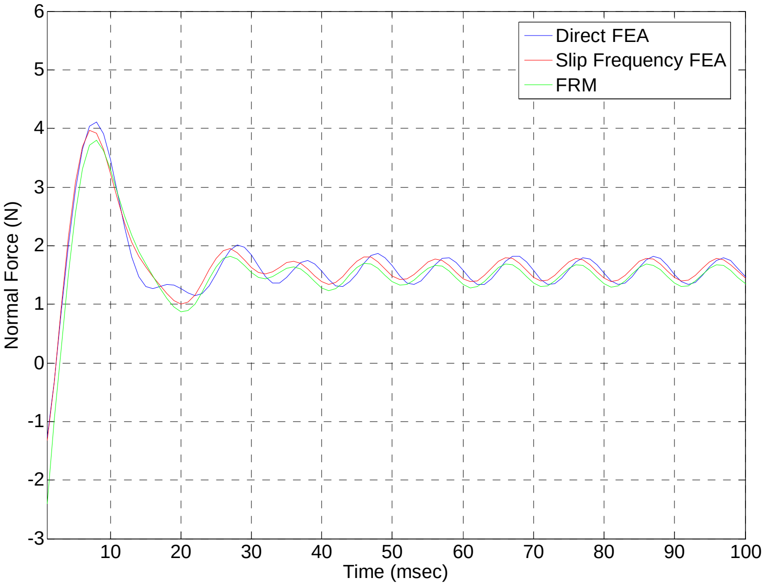

Figure 53 Normal Force Variations of Three Methods

3.5 Saturation Effects

No saturation is one of the fundamental assumptions of FRM. However, it is necessary to investigate the robustness of FRM to saturation effects. The comparison in the last session is repeated here. Except the current amplitude, all the other parameters are the same. In FEA calculation and FRM, the phase current amplitude is changed to 25 A, such that the maximum flux density in primary of LIM is about 1.49 T. This means the machine has been saturated. Figure 54 and 55 illustrate the flux densities from both slip frequency FEA and FRM at instant 0.1 sec. One can notice there is some local visual difference between the results from slip frequency FEA and FRM due to the existence of saturation effect. However, most part of the waveform matches well.

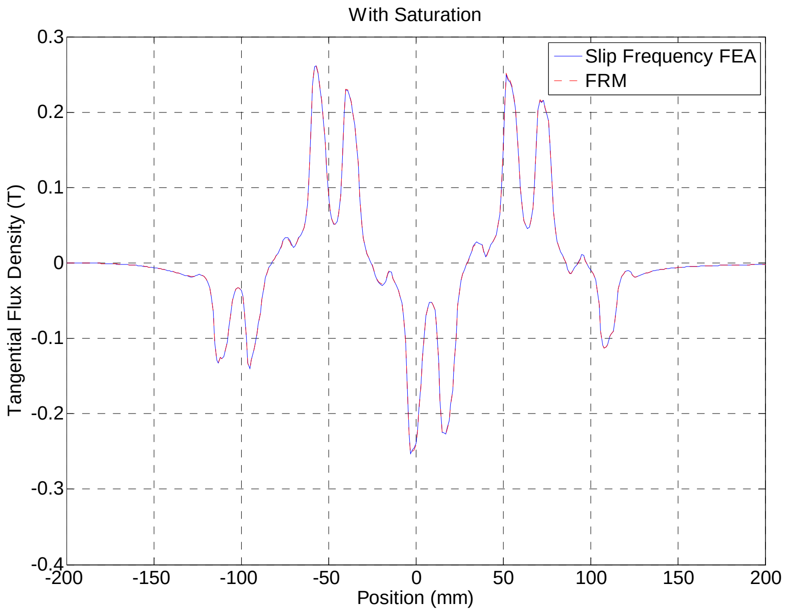

Figure 54 Tangential Flux Density with Saturation

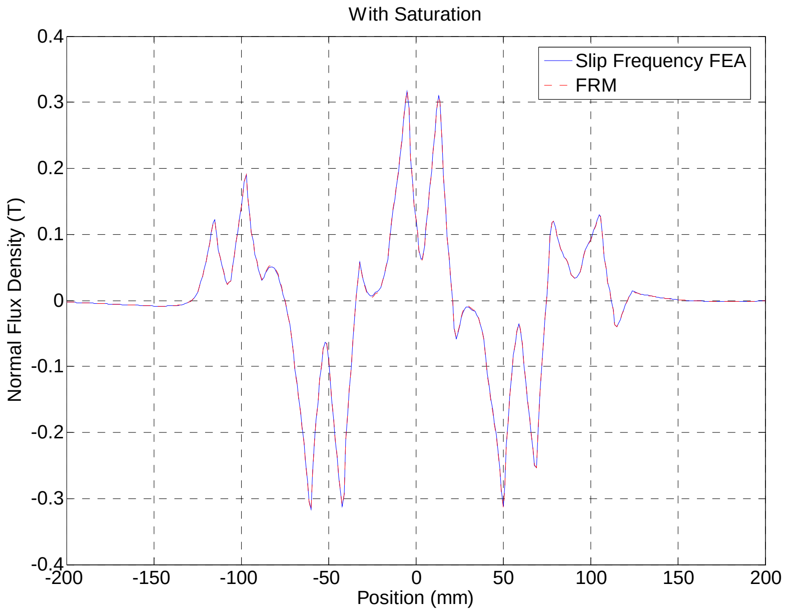

Figure 55 Normal Flux Density with Saturation

Figure 56 and 57 represent the resultant force profiles subject to the saturation effects. One can notice that the steady state dc errors between the three methods increase to 2.5%. FRM can still generate accurate enough results even though the saturation is existing.

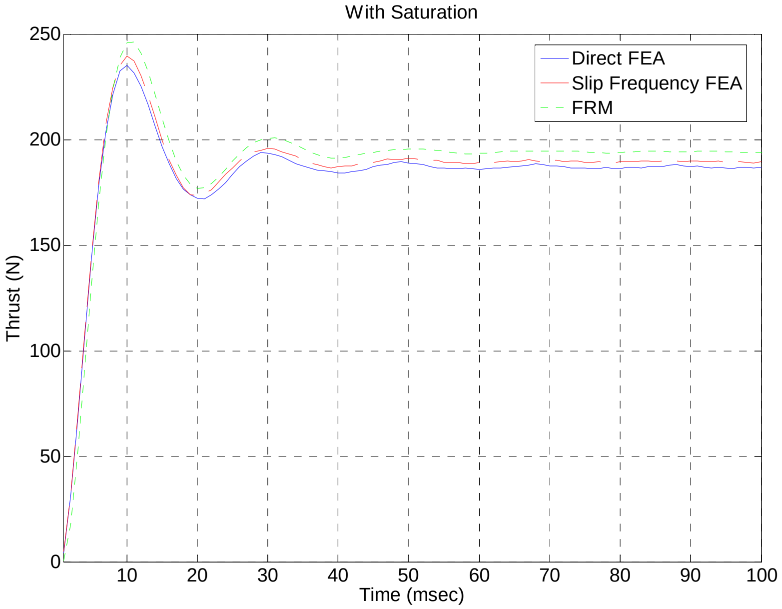

Figure 56 Thrust Variations of Three Methods with Saturation

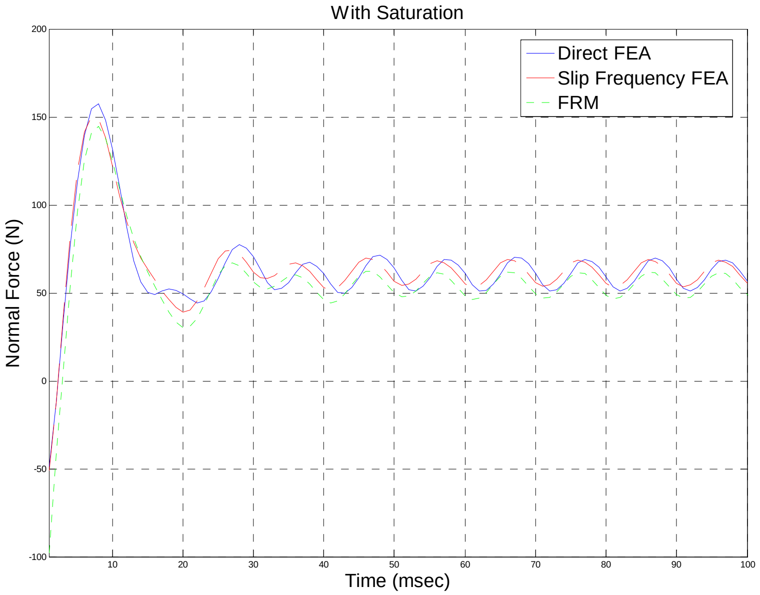

Figure 57 Normal Force Variations of Three Methods with Saturation

CHAPTER 4

INDIRECT FIELD ORIENTED CONTROL OF LINEAR INDUCTION MACHINES

Direct field oriented control directly measures the location of rotor flux axis, and uses the flux angle to decouple the stator currents into quadrature and direct components, i.e. I_q and I_d. I_q and I_d are also called force and magnetizing current respectively. The concept of indirect field oriented control is similar to that of direct field oriented control in which the position of rotor flux in the airgap is estimated. The control core governed by equation (2) and (3) has been introduced in the chapter 2.

The following assumptions have been made for vector (field oriented) current control. The system is three phase balanced (or symmetric in space and time). In addition, the translational magneto-motive force is sinusoidal. Furthermore, the machine is not saturated.

Traditionally, for rotary induction motor drives vector control can guarantee fast response because the decoupled I_q and I_d are dc components and easy to be regulated by PI controllers. Since LIM inherent similarities with their rotary counterparts, vector control has been predominantly applied to LIM in the past. However, vector control does not deliver the maximum force per ampere performance. On the other hand, due to the existence of trailing eddy current effects and magnetic asymmetry effects, the first two fundamental assumptions on the sinusoidal magneto-motive field and lack of saturation have been undermined. This in turn influences the expected functionality of vector control. In the following sessions, details of indirect field oriented control (IFOC) will be explored.

4.1 Fundamentals of IFOC

Since IFOC does not need the two quadrature flux sensors to measure the rotor or stator flux, it is more often used. Figure 24 illustrates the block diagram of IFOC, which is based on equation (2) and (3) from chapter 2. These two equations are recalled here:

$$\omega_e = \frac{P}{2}\omega_r + \frac{1}{\tau_r}\frac{i_{qs}}{i_{ds}} \tag{2}$$

$$I_{rms} = \sqrt{(i_{qs})^2 + (i_{ds})^2} \tag{3}$$

In the diagram, L_M is the magnetizing inductance, L_{rr} is the secondary inductance, r_r is the secondary resistance, secondary time constant τ_r in equation (2) is defined as L_{rr} / r_r, θ_e is the flux angle used to decouple three phase stator current (*abc* axis) into *dq* axis and convert the quantities in *dq* axis back to *abc* axis. Under normal condition, i_{ds} will be regulated at its rated value, commanded i_{qs} is generated through the speed control loop. The thrust generated by the LIM drive can be expressed by the following two equations:

$$F_t = K_F i_{qs} \tag{24}$$

$$F_t = M\dot{v} + Dv + F_l \tag{25}$$

where F_t is the thrust, K_F is the force constant, M is the total mass of LIM primary system, D is the viscous friction coefficient, $\dot{v}$ is the acceleration speed, v is the linear speed.

4.1.1 Identification of Secondary Time Constant

From equation (2) it is observed that implementation of IFOC requires the LIM's secondary time constant τ_r. The time constant is determined by applying a DC current of 3A for a short period of time to establish a dc flux across the airgap and measuring the voltage across one of the excited phases and the third phase. The measured voltage when the source is removed appears due to the transient that develops in the secondary. On the removal of the source, the voltage drops and then rises to zero. The rising profile of the curve gives the time constant of the secondary which is about 40 msec. Figure 58 illustrates the experimental result of secondary time constant determination.

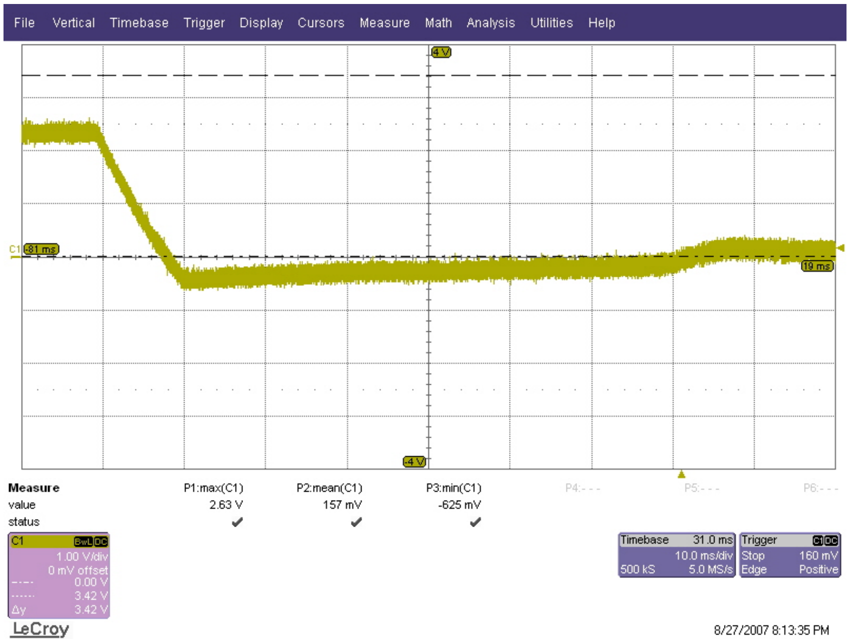

Measure	P1:max(C1)	P2:mean(C1)	P3:min(C1)	P4:- - -	P5:- - -	P6:- - -
value	2.63 V	157 mV	-625 mV			
status	✓	✓	✓			

C1 BwL DC
1.00 V/div
0 mV offset
–·–·– 0.00 V
······ 3.42 V
Δy 3.42 V

Timebase 31.0 ms
10.0 ms/div
500 kS 5.0 MS/s

Trigger C1 DC
Stop 160 mV
Edge Positive

8/27/2007 8:13:35 PM

Figure 58 Measurement of Secondary Time Constant (Vertical Axis: Voltage, Horizontal Axis: Time)

4.1.2 Determination of Parameters in dq Axis

In order to harvest the best performance that IFOC can supply, the accurate information of i_{ds}, i_{qs}, and K_F rated values needs to be identified. Equation (2) and (3) are utilized in this procedure.

At standstill and normal condition, equation (2) and (3) will be modified as equation (26) and (27) as follows:

$$\omega_e = \frac{1}{\tau_r}\frac{i_{qs}^r}{i_{ds}^r} \tag{26}$$

$$I_{rms}^r = \sqrt{\left(i_{qs}^r\right)^2 + \left(i_{ds}^r\right)^2} \tag{27}$$

where i_{qs}^r, i_{ds}^r, and I_{rms}^r are the rated values of *dq* axis and phase currents respectively.

According to the specification of LIM, the rated phase current is 4 A, and rated thrust is 7 lbs (31.14 N). In addition, from FRM the maximum standstill thrust occurs when excitation frequency is 24.43 Hz. This frequency is the rated frequency at standstill. Based on this information, i_{qs}^r and i_{ds}^r can be estimated as following values:

i_{ds}^r=0.643 A, i_{qs}^r=3.948 A.

Furthermore, K_F can be identified as 8.042 N/A using equation (24).

4.2 Closed Loop Speed Control Using IFOC

In this session, closed loop speed control based on IFOC will be conducted. This includes simulation study and experiment verification.

4.2.1 Simulation Study of IFOC

In the closed loop speed control, i_{ds} is regulated at its rated value, i_{qs} is regulated such that it can develop the desired thrust to track the reference speed. Once i_{ds} and i_{qs} references are generated, they will be transformed back to *abc* axis to produce three phase current references. Furthermore, phase current is controlled using hysteresis control. Figure 59 illustrates the speed control loop of IFOC in Matlab/Simulink. It mainly comprises of PI controller, saturation block, and LIM plant. The bandwidth of PI controller should be much less than that of current controller due to the fact that the mechanical system time constant is much larger. Therefore, i_{qs} reference can be used in the diagram instead of the real i_{qs} such that equation (24) can be modified as:

$$F_t = K_F i_{qs}^* \tag{28}$$

The block 'saturation' is used to prevent the i_{qs} exceeding its normal value. The total mass M of the LIM primary system is 17 Kg, and the viscous friction coefficient D is 0.05 N*sec/m.

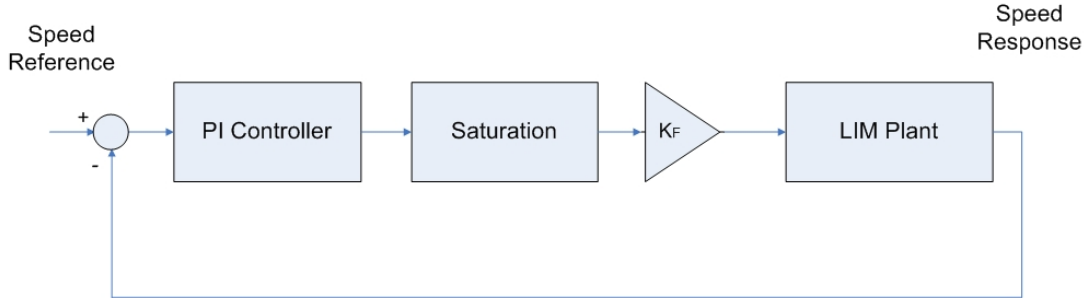

Figure 59 Block Diagram of Closed Loop Speed Control with IFOC

Based on figure 59, the characteristic equation of the speed control loop is formulated as follows:

$$1+\frac{k(s+a)}{s}*K_F*\frac{1}{17s+0.05}=0 \tag{29}$$

k is the proportion coefficient, a is the integration coefficient, and $1/(17s+0.05)$ is the plant of the LIM. The bandwidth of the PI controller is selected at 20 Hz, and the damping ratio is 0.9. Based on these parameters, k and a can be computed as 531.3 and 62.8 respectively. However, because of the non-linearity of the saturation block, k=80, and a=10 can give best simulation results by trial & error selection. Figure 60 represents the speed response from the simulation. Reference speed steps up to 0.1 m/sec at instant 0.2 sec. The reason that linear speed reference chooses 0.1 m/sec is that the length of the LIM secondary railway is limited. One can notice that there is an overshoot about 20% in the speed response, and speed reaches steady state in about 0.4 sec.

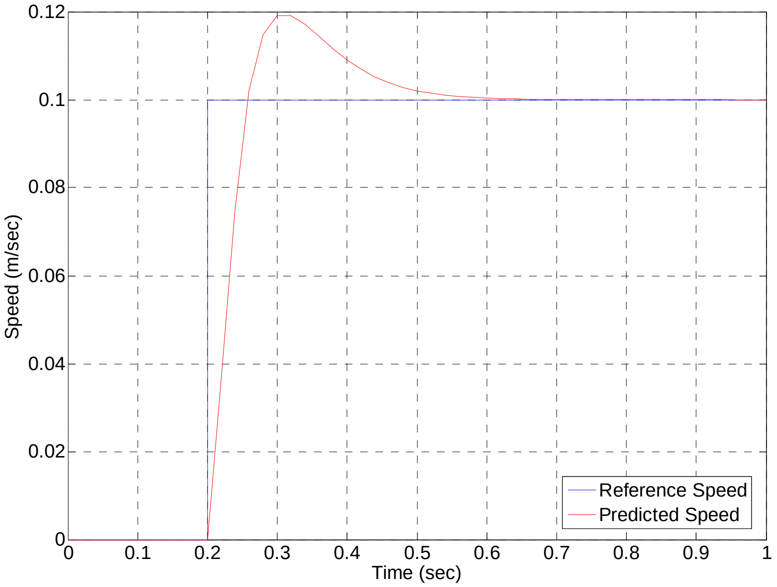

Figure 60 Speed Response of IFOC in Simulation

4.2.2 Experimental Verification of IFOC

In order to verify the functionality of designed speed controller for LIM using IFOC, experimental results will be shown in this section. Figure 61 illustrates the block diagram of hardware set up. The 'DC Power Supply' will supply a solid 30 V dc bus for the system; 'Protection Diode' is used to prevent the dc power supply absorbing current; dc link capacitor is a power buffer for regenerative braking. The control station collects the three phase current information and linear speed value, and generates a sequence of switching signals for the corresponding IGBT switches based on IFOC and current hysteresis control. The hysteresis band for the current controller is 0.06 A. Detailed configuration of hardware setup is shown in APPENDIX B.

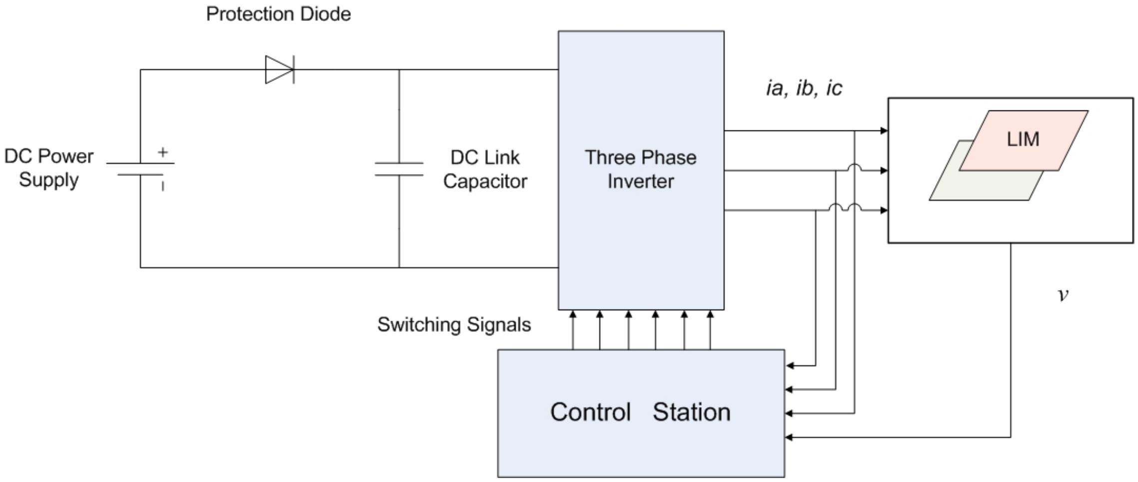

Figure 61 Block Diagram of Hardware Set Up

Figure 62 illustrates the speed response of a rectangular speed reference at no load condition. At instant 0 sec, speed reference steps up to 0.1 m/sec, and steps down to 0 at instant 3.072 sec. One can notice that it takes about 1.5 sec for the speed to reach its reference value when starting, and 1 sec when braking. This is because when starting the thrust overcomes the friction force; however, when braking thrust and friction force will sum together to decelerate the system. In addition, for the initial starting period 0.5 sec, the speed does not change much, that is because the period is utilized for LIM to overcome the static friction force. Figure 63-65 represent the phase current during starting, mode transition, and braking under no load condition. One can observe that when LIM is starting or braking, phase current maintains amplitude of 4 A to generate the maximum thrust to drive the system. Figure 64 illustrates that in steady state when linear speed reaches its reference value, the commanded force current i_{qs}^{*} varnishes, as a result, the amplitude of phase current decreases. Thereafter, the operation mode switches.

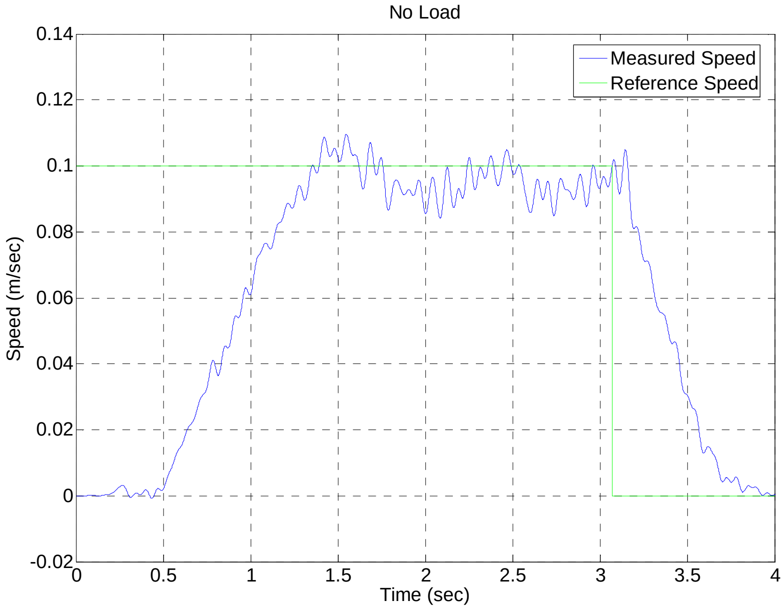

Figure 62 Speed Response of IFOC from Experiment (No Load)

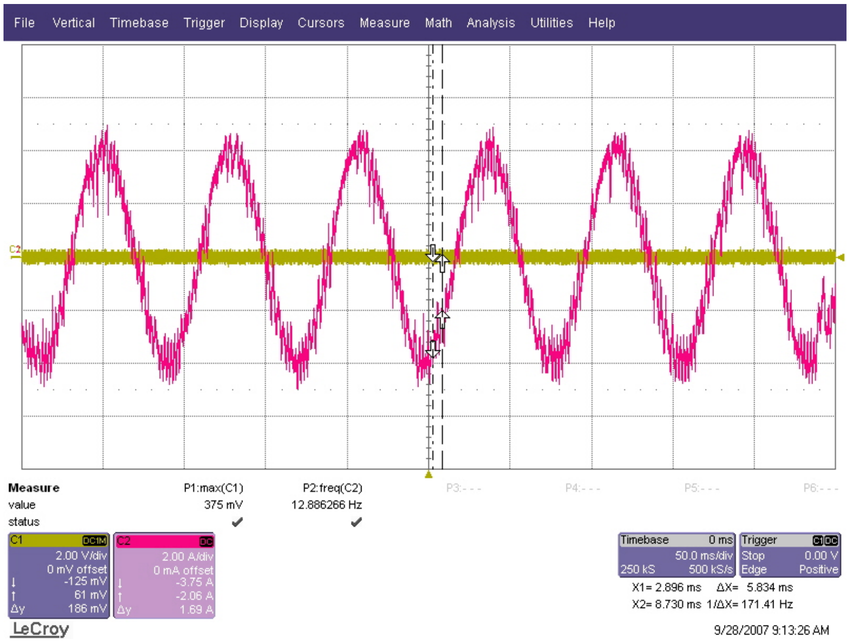

Measure	P1:max(C1)	P2:freq(C2)	P3:- - -	P4:- - -	P5:- - -	P6:- - -
value	375 mV	12.886266 Hz				
status	✓	✓				

C1 DC1M
2.00 V/div
0 mV offset
↓ -125 mV
↑ 61 mV
Δy 186 mV

C2 DC
2.00 A/div
0 mA offset
↓ -3.75 A
↑ -2.06 A
Δy 1.69 A

Timebase 0 ms
50.0 ms/div
250 kS 500 kS/s

Trigger C1 DC
Stop 0.00 V
Edge Positive

X1= 2.896 ms ΔX= 5.834 ms
X2= 8.730 ms 1/ΔX= 171.41 Hz

9/28/2007 9:13:26 AM

Figure 63 Phase Starting Current of IFOC (No Load)

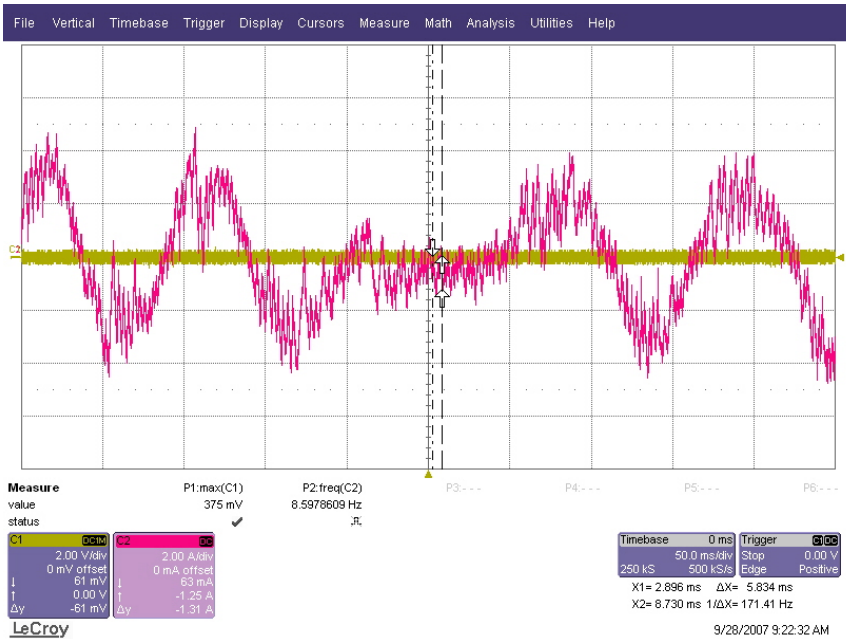

Figure 64 Transition of Operation Mode of Phase Current in IFOC (No Load)

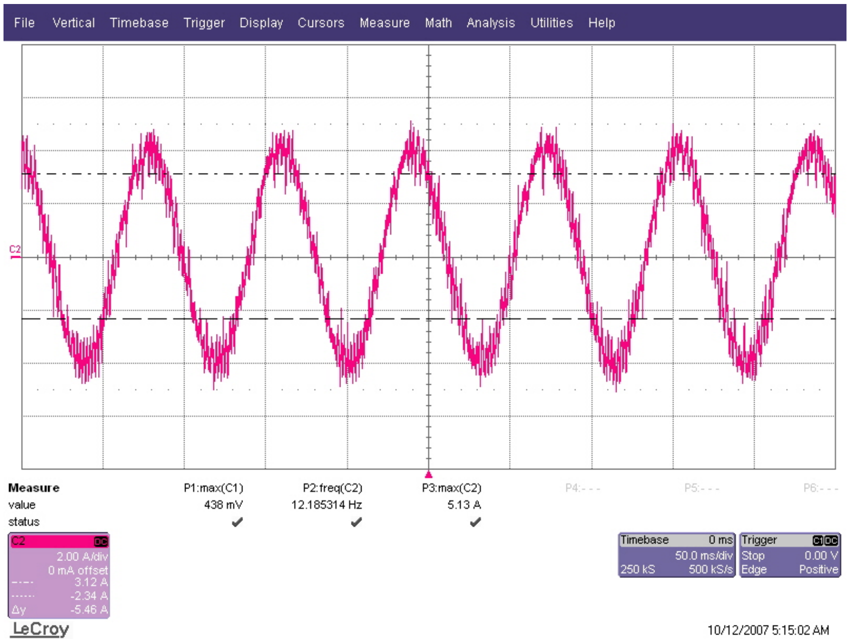

Figure 65 Phase Braking Current of IFOC (No Load)

Figure 66 illustrates the speed response of a rectangular speed reference when a 22 lbs mass is put on top of the primary to increase the friction force and time constant of the mechanical system. One can notice that compared with no load condition both slopes of starting and braking are reduced, because the total mass of primary is increased. From figure 62 and 66, one can observe that in steady state there is a dc error between the reference speed and measured speed. This is mainly because of the trailing eddy current effects and magnetic asymmetry effects. In addition, the performance of the speed controller is restricted by the order of the speed controller.

Figure 67-69 illustrate the phase current during starting, mode transition, and braking when LIM is loaded by the 22 lbs mass. It can be noticed that the profiles of phase current when the machine is loaded are very similar to those under no load condition. In addition, there is certain amount of noise in the current waveform. This is mainly because the excitation frequency not only depends on linear speeds, but also relies on the i_{qs}. However, i_{qs} is also a function of linear speed. Therefore, the resultant excitation frequency will suffer from two sources of noise.

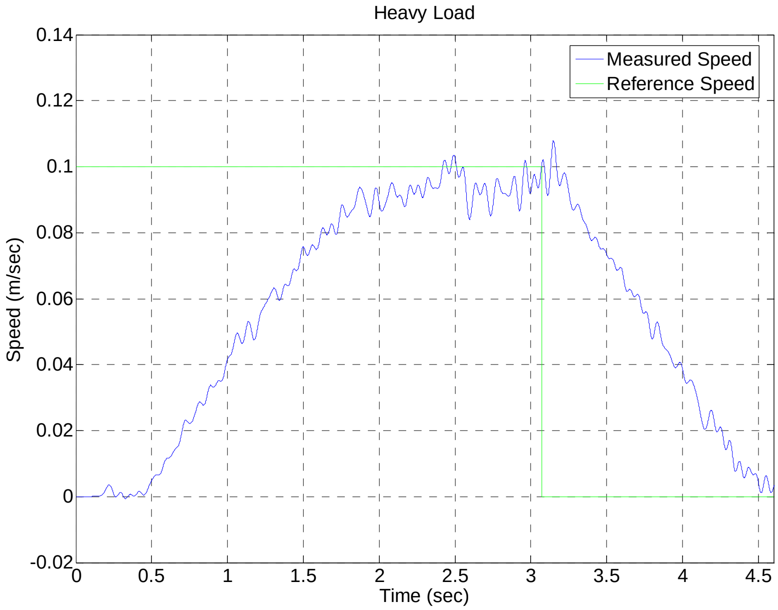

Figure 66 Speed Response of IFOC from Experiment (22 lbs Load)

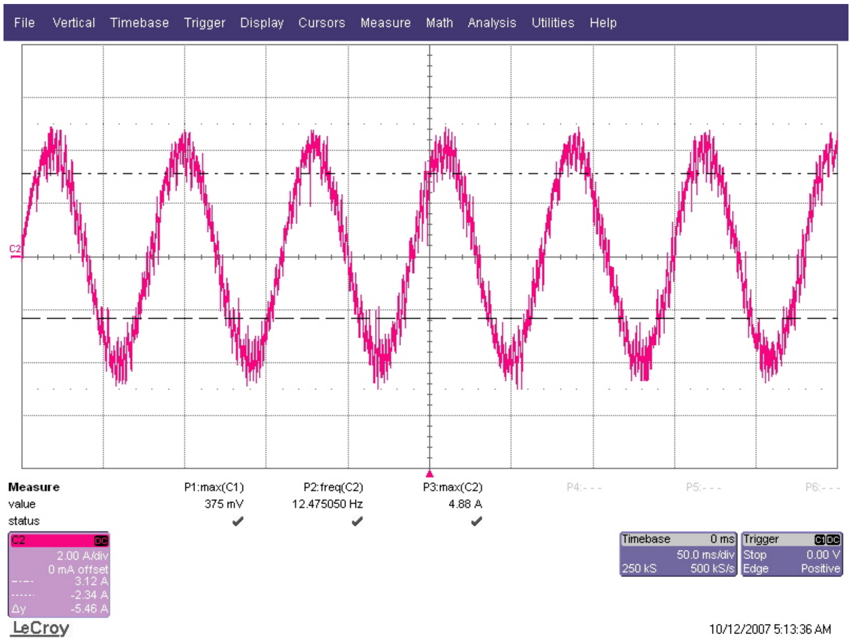

Measure	P1:max(C1)	P2:freq(C2)	P3:max(C2)	P4:- - -	P5:- - -	P6:- - -
value	375 mV	12.475050 Hz	4.88 A			
status	✓	✓	✓			

C2 DC
2.00 A/div
0 mA offset
-·-·- 3.12 A
······ -2.34 A
Δy -5.46 A

Timebase 0 ms
50.0 ms/div
250 kS 500 kS/s

Trigger C1 DC
Stop 0.00 V
Edge Positive

10/12/2007 5:13:36 AM

Figure 67 Phase Starting Current of IFOC (22 lbs Load)

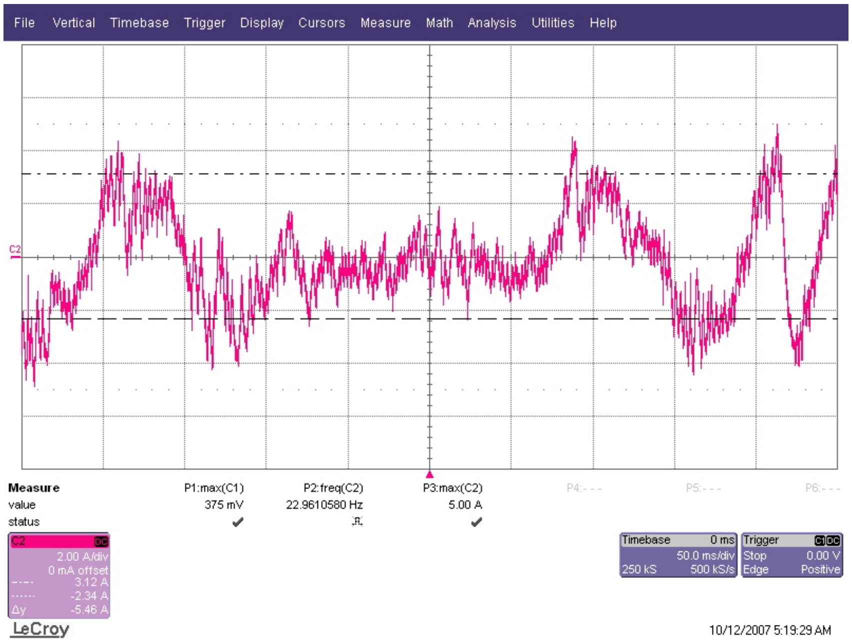

Measure	P1:max(C1)	P2:freq(C2)	P3:max(C2)	P4:- - -	P5:- - -	P6:- - -
value	375 mV	22.9610580 Hz	5.00 A			
status	✓		✓			

C2 DC
2.00 A/div
0 mA offset
3.12 A
-2.34 A
Δy -5.46 A

Timebase 0 ms
50.0 ms/div
250 kS 500 kS/s

Trigger C1 DC
Stop 0.00 V
Edge Positive

10/12/2007 5:19:29 AM

Figure 68 Transition of Operation Mode of Phase Current in IFOC (22 lbs Load)

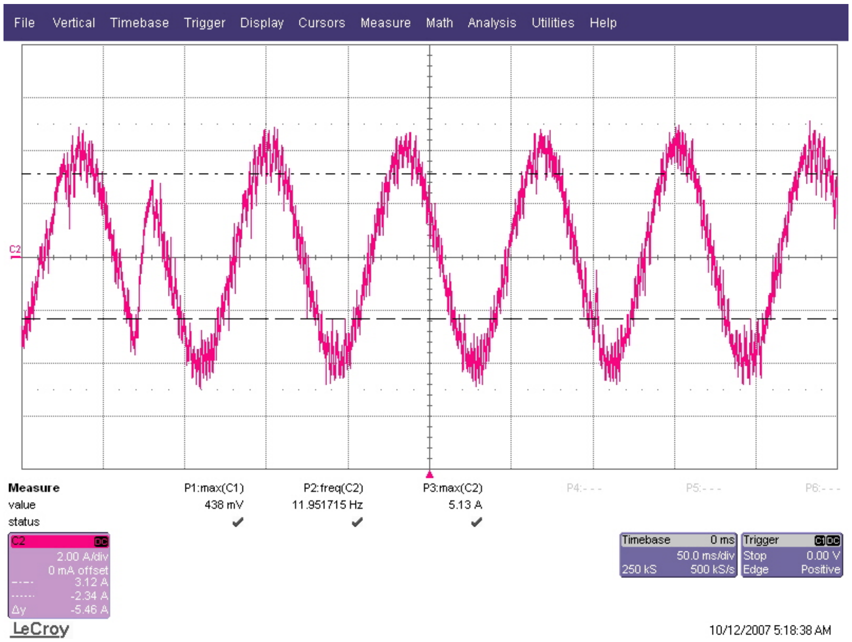

Measure	P1:max(C1)	P2:freq(C2)	P3:max(C2)	P4:- - -	P5:- - -	P6:- - -
value	438 mV	11.951715 Hz	5.13 A			
status	✓	✓	✓			

C2 DC
2.00 A/div
0 mA offset
3.12 A
-2.34 A
Δy -5.46 A

Timebase 0 ms
50.0 ms/div
250 kS 500 kS/s

Trigger C1 DC
Stop 0.00 V
Edge Positive

10/12/2007 5:18:38 AM

Figure 69 Phase Braking Current of IFOC (22 lbs Load)

CHAPTER 5

MAXIMUM FORCE PER AMPERE CONTROL OF LINEAR INDUCTION MACHINES

Since the trailing eddy current effects and magnetic asymmetry effects have prevented IFOC of LIM harvesting its high grade performance, a simple, easy to implement, and fast response control strategy so called maximum force/ampere control is proposed and implemented in this chapter.

5.1 Principles of Maximum Force per Ampere Control

Figure 70 and 71 illustrate the average thrust and normal force variations with respect to primary frequency at different linear speeds. One can notice that at any linear speed, there is always one pair of excitation frequencies that can produce the maximum driving force or braking force for the LIM system. These frequencies are characterized as optimum frequencies. If the gravity force and its by-product, friction force, are also taken into account, one can summarize the following expression:

$$F_t - \xi_{friction}(M \times g + F_n) = M \times a \tag{30}$$

where F_t is the thrust force, F_n is the normal force, $\xi_{friction}$ is the friction coefficient between LIM and supporting frame, g is the gravity constant, M is total mass of the LIM system, and a is the acceleration speed of the whole system. Using FRM, one can always find the pair of optimum frequencies for each linear speed. For example, when linear speed is 5 m/sec, the optimum frequency of motoring is 77.49 Hz, and optimum frequency of generating is 25.9 Hz.

Based on the knowledge of the optimum frequencies for the discrete linear speeds and interpolation method, lookup tables between linear speed and optimum frequency under motoring and generating conditions can be set up. Furthermore, the optimum frequency is fed into the power converter to produce a set of three phase, balanced, current sources of optimum frequencies using hysteresis control. As a result, at any linear speed maximum force/ampere can be guaranteed. Finally, linear speed is regulated with the usage of hysteresis control. The complete functionality of the maximum force/ampere control is shown in figure 72. As shown in figure 72, hysteresis comparator in the block diagram determines whether the machine should work as a motor or as a generator. This information will be given to the block called 'Frequency Selector'. Two lookup tables store the optimum frequencies at discrete linear speeds. One of the outputs from the lookup tables will be selected based on the operation mode. The following two expressions can explain the function of 'Frequency Selector' in details:

$$f_{\_out} = f_{\_in}(motoring), \text{ if } Speed_{\_ref} - Speed_{\_out} > Hysteresis\ band \qquad (31)$$

$$f_{\_out} = f_{\_in}(generating), \text{ if } Speed_{\_ref} - Speed_{\_out} < -Hysteresis\ band \qquad (32)$$

where $f_{\_out}$ is the output of the frequency selector, $f_{\_in}(motoring)$ and $f_{\_in}(generating)$ are the outputs of the two lookup tables, $Speed_{\_ref}$ is the reference linear speed, and $Speed_{\_out}$ is the measured linear speed.

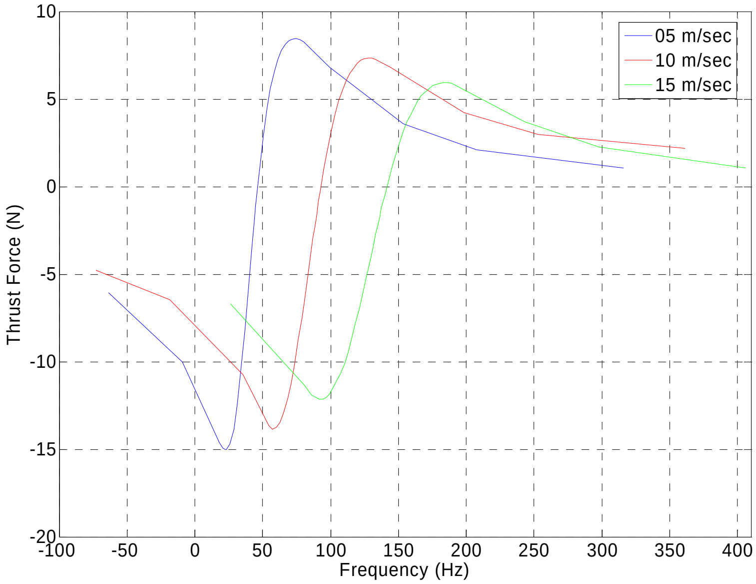

Figure 70 Average Thrust Variation with Excitation Frequency at Different Linear Speeds

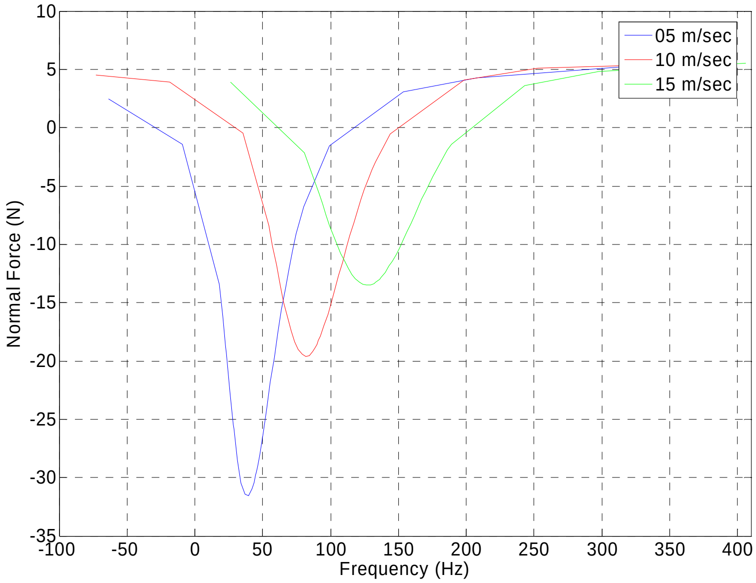

Figure 71 Average Normal Force Variation with Excitation Frequency at Different Linear Speeds

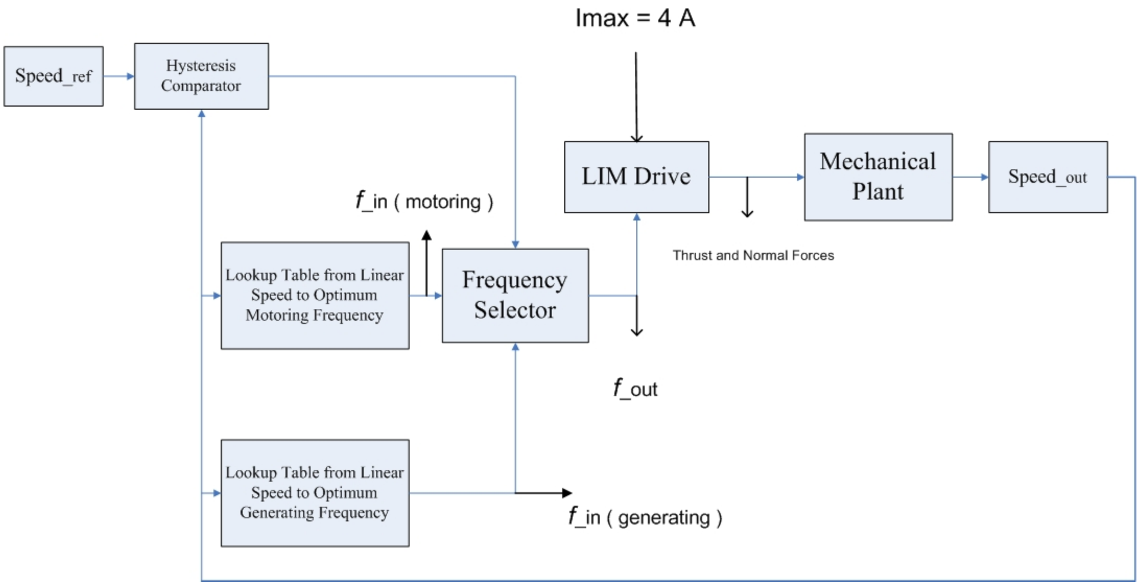

Figure 72 Control Block Diagram for the Maximum Force/Ampere Control

5.2 Simulation Study of Maximum Force per Ampere Control

Figure 73 represents the speed response of a rectangular reference speed. At instant 0.2 sec, speed reference steps up to 0.1 m/sec, and steps down to zero at instant 0.8 sec. The hysteresis band of the speed regulator is 0.01 m/sec. It is notable that under accelerating condition, the friction force resists motion; however, under decelerating condition, the friction force helps the braking. Therefore, figure 73 has larger braking slope than the one of starting. This is very similar to the phenomenon of figure 62 and 66.

Figure 74 is the simulated optimum excitation frequency profile. It can be observed that depending on the mode of operation, frequency switches between motoring (positive frequency) and generating (negative frequency) conditions.

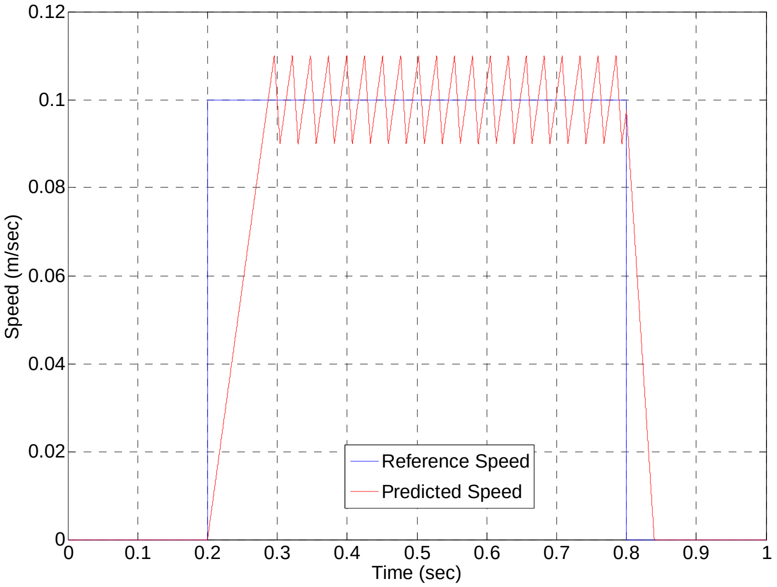

Figure 73 Speed Response of Maximum Force/Ampere Control

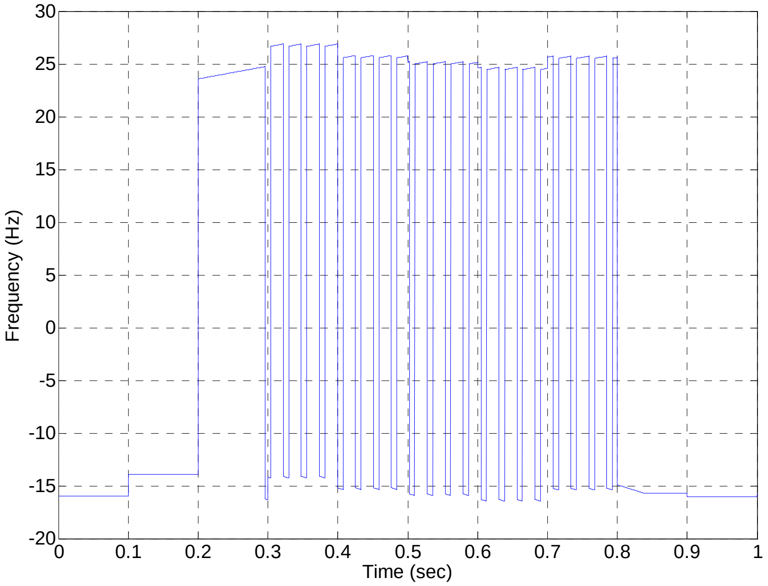

Figure 74 Profile of Optimum Excitation Frequency

Figure 75 illustrates the reference phase current and the predicted phase current using hysteresis control. Figure 76 is the zoomed version of figure 75.

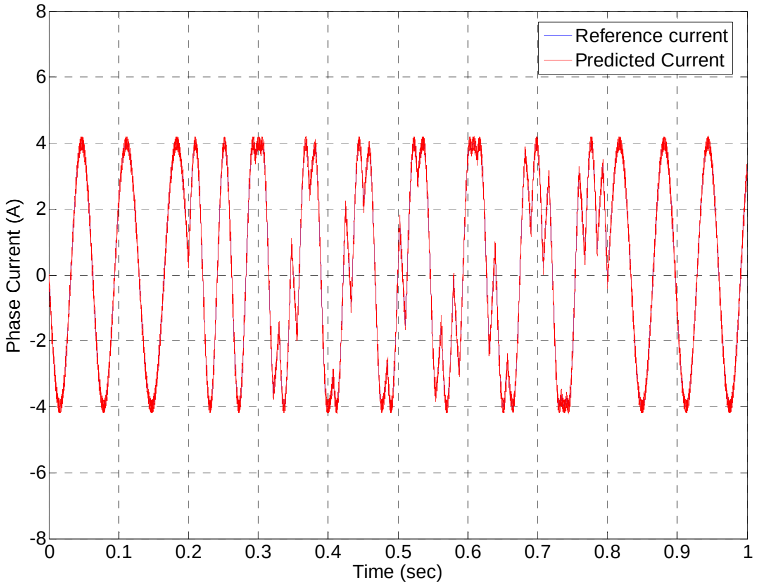

Figure 75 Simulated Reference Phase Current and Predicted Phase Current

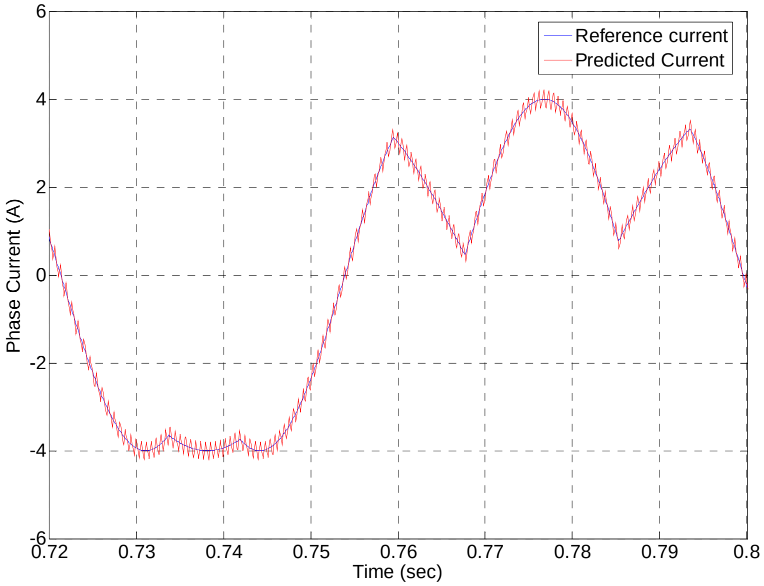

Figure 76 Zoomed Phase Current Profile

Figure 77 and 78 represent the thrust and normal force ripples with respect to frequency at linear speed of 5 m/sec. One can notice there is one peak in figure 77. The reason is that when linear speed approaches synchronous speed, the thrust approaches zero. As a result, even a small value of ripple in the force will cause an extremely large thrust ripple percentage. However, there are two peaks in figure 78. The reason of the peak in the negative frequency is that when frequency approaches negative infinity or positive infinity, normal force changes to repulsion force from attraction force [20]. When normal force is zero, the normal force ripple percentage will be infinity. The second peak happens when thrust force ripple percentage has a minimum value. When linear speed is 5 m/sec, the optimum frequency of motoring is 77.49 Hz, and optimum frequency of generating is 25.9 Hz. Both of these two frequencies will generate relatively small force ripples at this linear speed. This means that the maximum force/ampere control has good immunity with respect to force noise.

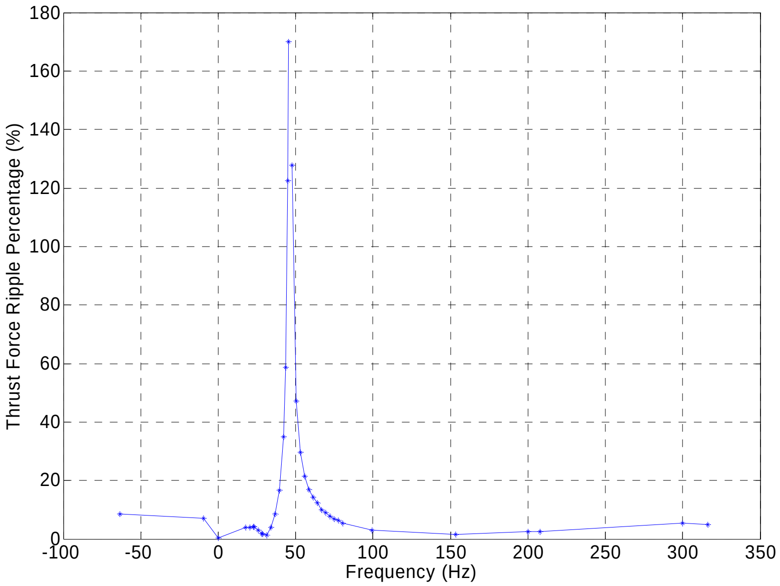

Figure 77 Thrust Ripple Percentage with Respect to Frequency at Linear Speed 5 m/sec

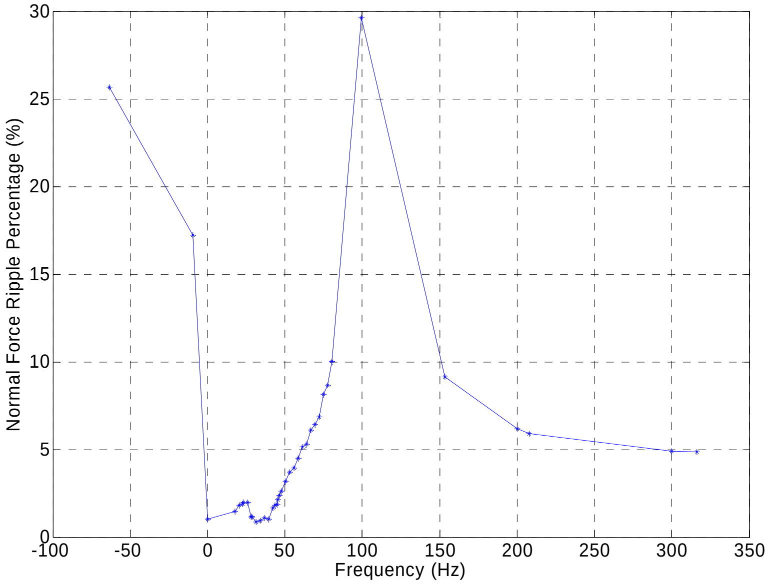

Figure 78 Normal Force Ripple Percentage with Respect to Frequency at Linear Speed 5 m/sec

In the session 2.4 and 2.5, the impact of airgap length and secondary electric conductivity effect has already been explored. It is necessary to investigate whether the maximum force/ampere control can tolerate the airgap length and secondary electric conductivity variations. Figures 79 and 80 represent the thrust and normal force variations with respect to excitation frequency when airgap is set at 2.5 mm and 4.5 mm respectively (linear velocity is 10 m/sec). It can be observed that when airgap length discrepancy is 80% to the rated value 2.5 mm, the pair of optimum frequencies at 10 m/sec linear speed do not change. This observation validates that the proposed control has good immunity to airgap length variation.

Due to the existence of heating effect of secondary reaction plate, the electric conductivity of aluminium plate will change. For instance, 20% discrepancy of the electric conductivity will result in the real electric conductivity being 31000000 Siemens/m (79% of Aluminum electric conductivity). Figures 81 and 82 illustrate the force variations with respect to excitation frequency when secondary electric conductivity is 39000000 Siemens/m (100% of Aluminum electric conductivity) and 31000000 Siemens/m respectively. One can notice that the pair of optimum frequencies for motoring and generating almost remains the same. Therefore, the proposed maximum force/ampere control is verified to tolerate the secondary heating effect well.

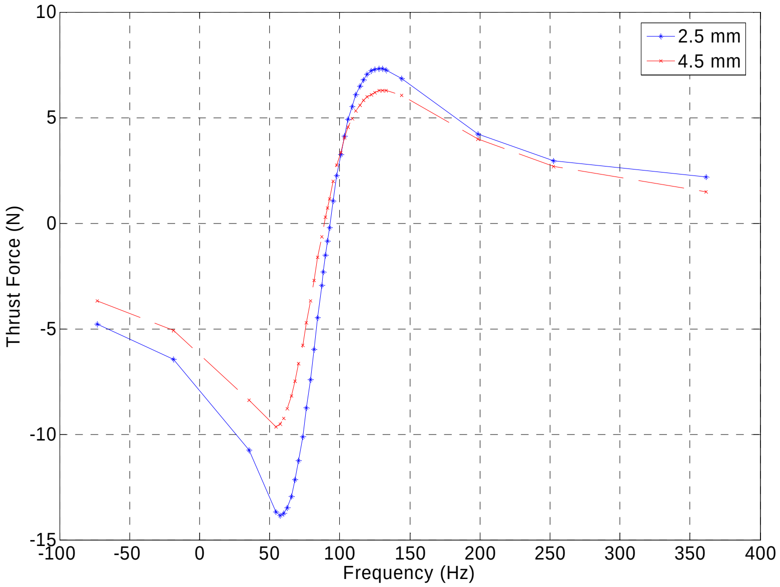

Figure 79 Thrust Variations with Excitation Frequency for Two Airgap Lengths when Linear Speed is 10 m/sec

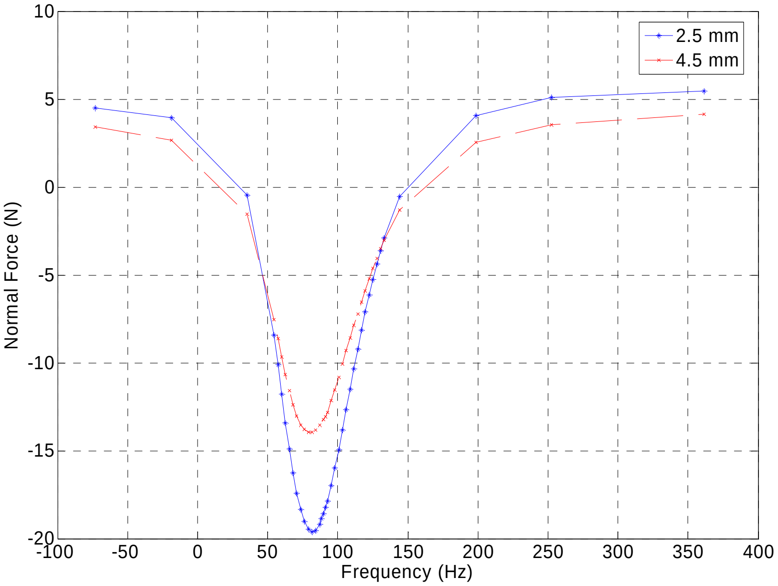

Figure 80 Normal Force Variations with Excitation Frequency for Two Airgap Lengths when Linear Speed is 10 m/sec

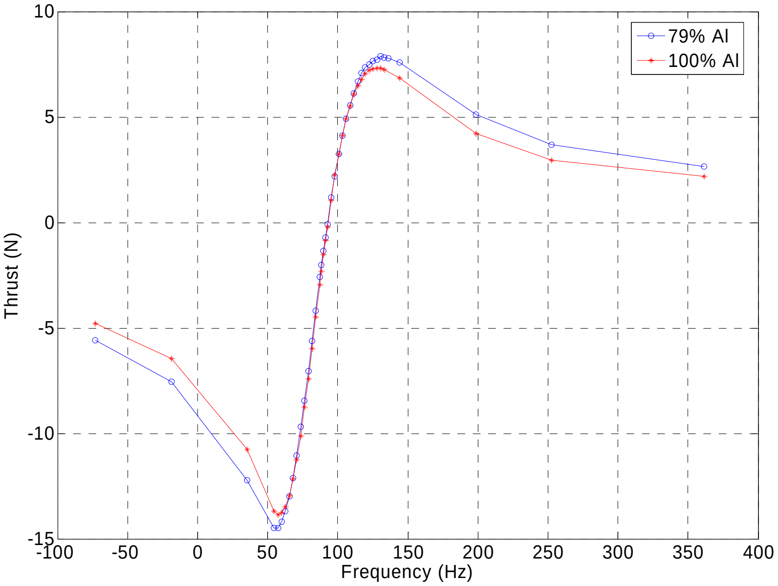

Figure 81 Thrust Variations with Excitation Frequency for Two Secondary Electric Conductivity Values

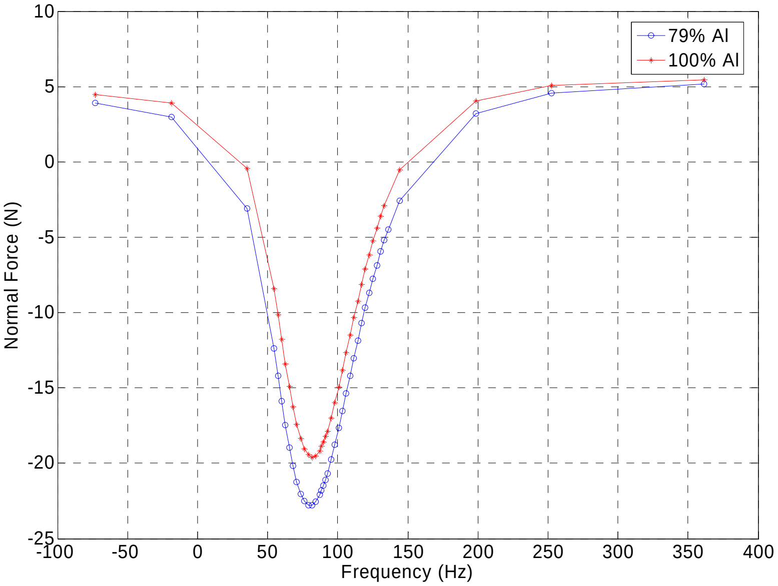

Figure 82 Normal Force Variations with Excitation Frequency for Two Secondary Electric Conductivity Values

5.3 Experimental Verification of Maximum Force per Ampere Control

Figure 83 illustrates the speed response under no load condition using maximum force/ampere control. One can notice that when speed reference steps up to 0.1 m/sec at 0 sec, the speed response is tracking the reference immediately. In addition, the maximum force/ampere control has excellent speed regulation in steady state. Furthermore, the braking slope is larger than that of starting.

Figure 84-86 illustrate the transition of phase current from starting to steady state, from steady state to braking, and during steady state. Figure 86 verifies that during steady state, depending on the operation mode, excitation frequency switches. In addition, it has very similar format with the simulated waveform. Furthermore, the current waveform has less noise than the current waveform from IFOC, because the excitation frequency in maximum force/ampere control only depends on linear speed once.

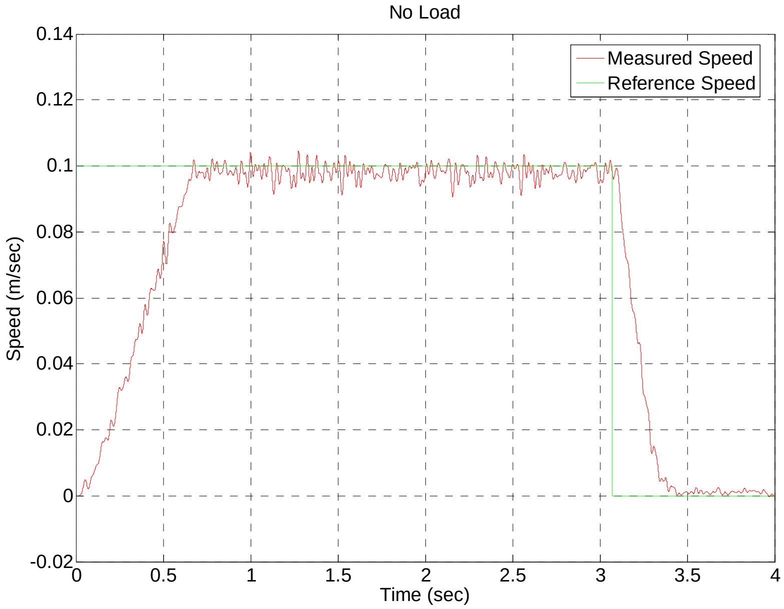

Figure 83 Speed Response of Maximum Force/Ampere Control (No Load)

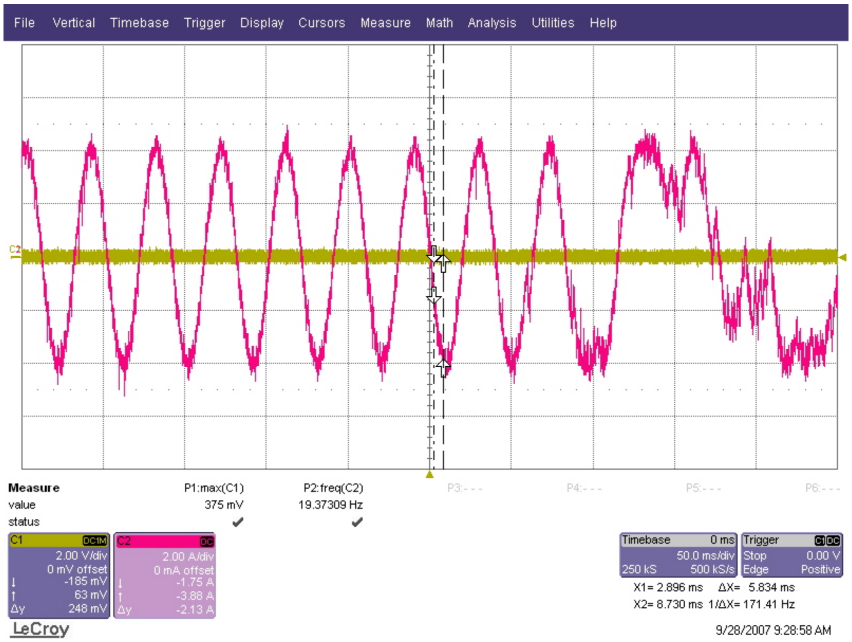

```
Measure     P1:max(C1)   P2:freq(C2)   P3:- - -   P4:- - -   P5:- - -   P6:- - -
value           375 mV   19.37309 Hz
status               ✓             ✓

C1           DC1M    C2             DC                       Timebase        0 ms   Trigger      C1DC
       2.00 V/div           2.00 A/div                                 50.0 ms/div  Stop        0.00 V
    0 mV offset          0 mA offset                        250 kS     500 kS/s     Edge      Positive
↓      -185 mV       ↓       -1.75 A                          X1= 2.896 ms    ΔX=  5.834 ms
↑        63 mV       ↑       -3.88 A                          X2= 8.730 ms  1/ΔX= 171.41 Hz
Δy      248 mV       Δy      -2.13 A

                                                                          9/28/2007 9:28:58 AM
```

Figure 84 Transition Phase Current from Starting to Steady State (No Load)

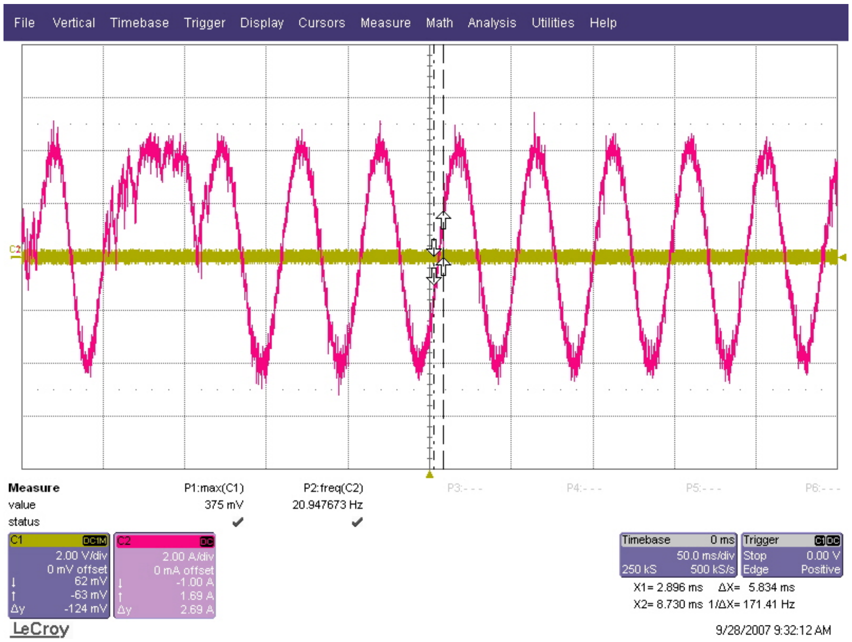

Measure P1:max(C1) P2:freq(C2)
value 375 mV 20.947673 Hz
status ✓ ✓

C1 DC1M
2.00 V/div
0 mV offset
↓ 62 mV
↑ -63 mV
Δy -124 mV

C2 DC
2.00 A/div
0 mA offset
↓ -1.00 A
↑ 1.69 A
Δy 2.69 A

Timebase 0 ms
50.0 ms/div
250 kS 500 kS/s

Trigger C1 DC
Stop 0.00 V
Edge Positive

X1= 2.896 ms ΔX= 5.834 ms
X2= 8.730 ms 1/ΔX= 171.41 Hz

9/28/2007 9:32:12 AM

Figure 85 Transition Phase Current from Steady State to Braking (No Load)

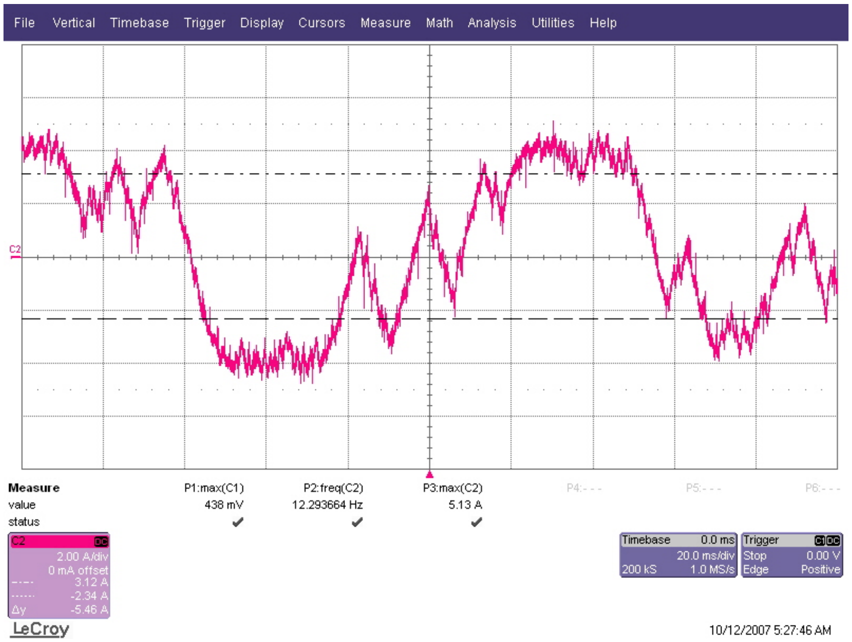

Measure P1:max(C1) P2:freq(C2) P3:max(C2)
value 438 mV 12.293664 Hz 5.13 A
status ✓ ✓ ✓

C2 DC
2.00 A/div
0 mA offset
-·-·- 3.12 A
······ -2.34 A
Δy -5.46 A

Timebase 0.0 ms
20.0 ms/div
200 kS 1.0 MS/s

Trigger C1 DC
Stop 0.00 V
Edge Positive

10/12/2007 5:27:46 AM

Figure 86 Zoomed Steady State Phase Current Using Maximum Force/Ampere Control (No Load)

Figure 87 represents the speed response when the primary is loaded with 22 lbs mass. Again, the steady state speed is still regulated well with small ripples. Figure 88-90 display the transition of phase current from starting to steady state, from steady state to braking, and during steady state with 22 lbs load.

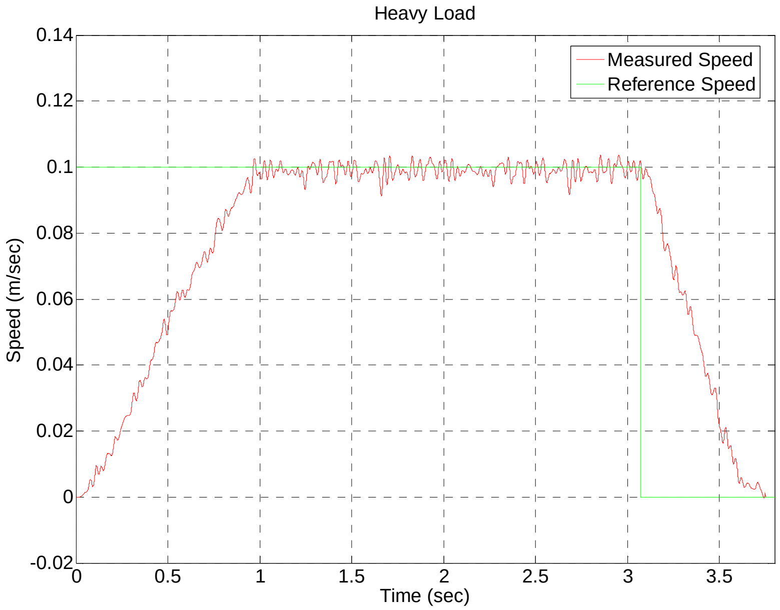

Figure 87 Speed Response of Maximum Force/Ampere Control (22 lbs Load)

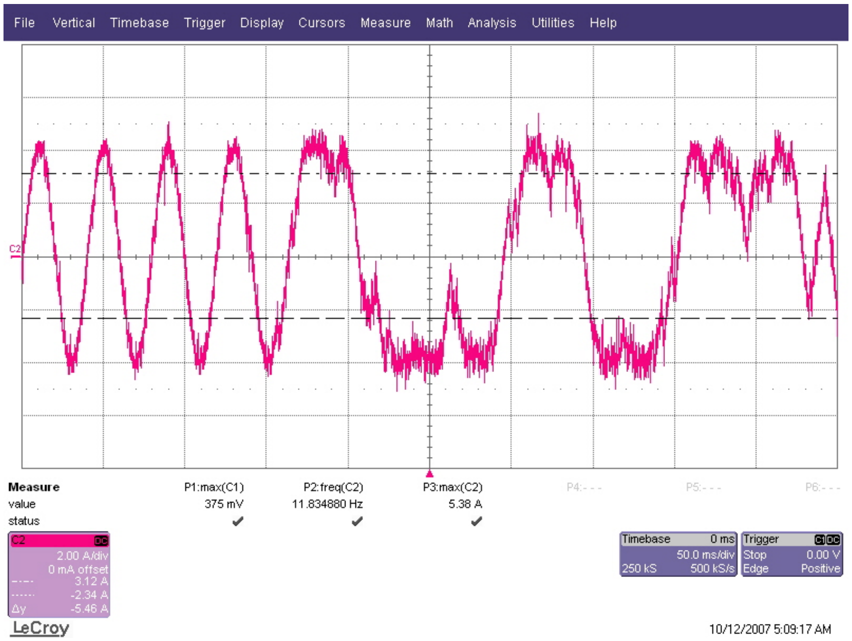

Measure P1:max(C1) P2:freq(C2) P3:max(C2) P4:- - - P5:- - - P6:- - -
value 375 mV 11.834880 Hz 5.38 A
status ✓ ✓ ✓

C2 DC
2.00 A/div
0 mA offset
3.12 A
-2.34 A
Δy -5.46 A

Timebase 0 ms
50.0 ms/div
250 kS 500 kS/s

Trigger C1 DC
Stop 0.00 V
Edge Positive

10/12/2007 5:09:17 AM

Figure 88 Transition Phase Current from Starting to Steady State (22 lbs Load)

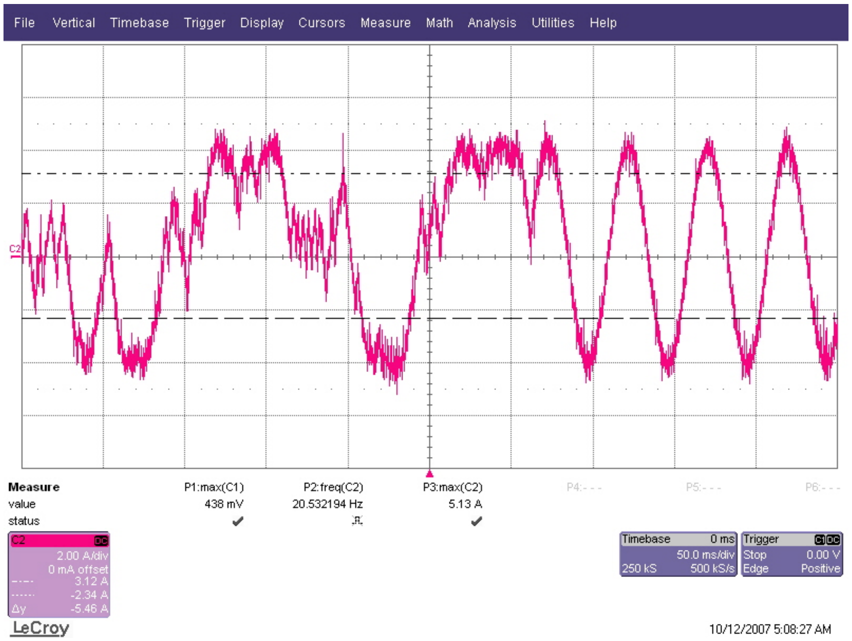

Measure P1:max(C1) P2:freq(C2) P3:max(C2) P4:- - - P5:- - - P6:- - -
value 438 mV 20.532194 Hz 5.13 A
status ✓ ✓

C2 DC
2.00 A/div
0 mA offset
3.12 A
-2.34 A
Δy -5.46 A

Timebase 0 ms
50.0 ms/div
250 kS 500 kS/s

Trigger C1 DC
Stop 0.00 V
Edge Positive

10/12/2007 5:08:27 AM

Figure 89 Transition Phase Current from Steady State to Braking (22 lbs Load)

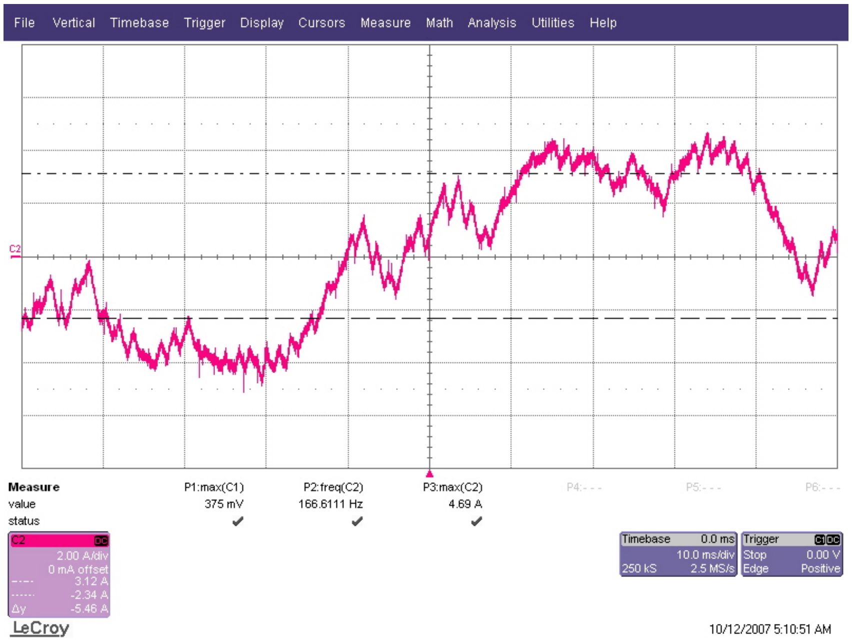

Measure	P1:max(C1)	P2:freq(C2)	P3:max(C2)	P4:- - -	P5:- - -	P6:- - -
value	375 mV	166.6111 Hz	4.69 A			
status	✓	✓	✓			

C2 DC
2.00 A/div
0 mA offset
3.12 A
-2.34 A
Δy -5.46 A

Timebase 0.0 ms
10.0 ms/div
250 kS 2.5 MS/s

Trigger C1 DC
Stop 0.00 V
Edge Positive

10/12/2007 5:10:51 AM

Figure 90 Zoomed Steady State Phase Current Using Maximum Force/Ampere Control (22 lbs Load)

5.4 Comparison between IFOC and Maximum Force per Ampere Control

As can be seen, the speed response of both methods is plotted together in figure 91 and 92. It can be seen that maximum force/ampere control has faster response and better regulation on the linear speed.

In addition, the current waveforms from maximum force/ampere control are much cleaner than those from IFOC. This will result in a smaller value of THD (total harmonic distortion).

Furthermore, it is necessary to investigate the stability and robustness of the two methods. Figure 93 and 94 illustrate the linear speed reaction when the 22 lbs mass is suddenly put on the moving primary in the steady state. In figure 93, at the instant about 0.1 sec, the load is put on the primary, there is a big dip in the speed profile. This is because the design of the PI controller for IFOC is based on the no load LIM plant (17 Kg). The sudden change of load will change the plant immediately. In figure 94, at the instant about 0.3 sec, the mass is put on the primary, however, the linear speed is not affected by this disturbance much. The reason is that at any instant the maximum force/ampere control always generates the maximum force per ampere based on the current linear speed value.

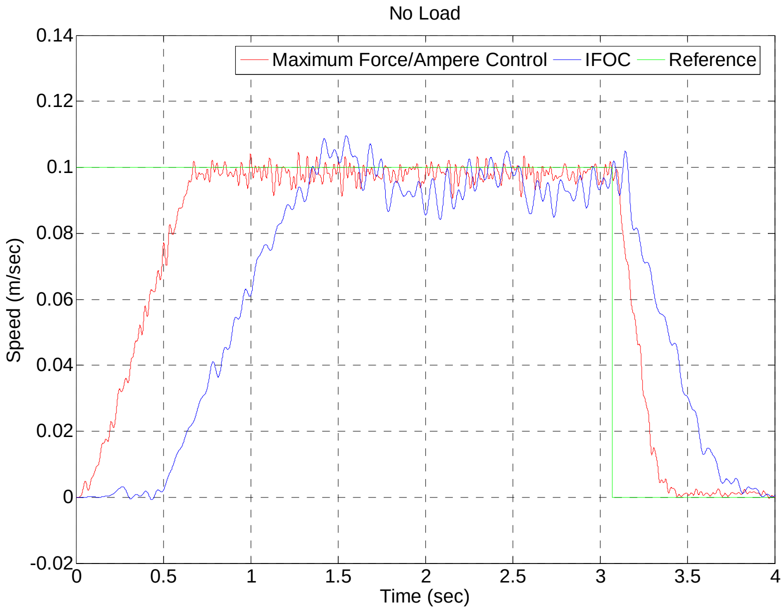

Figure 91 Speed Response of Both Methods (No Load)

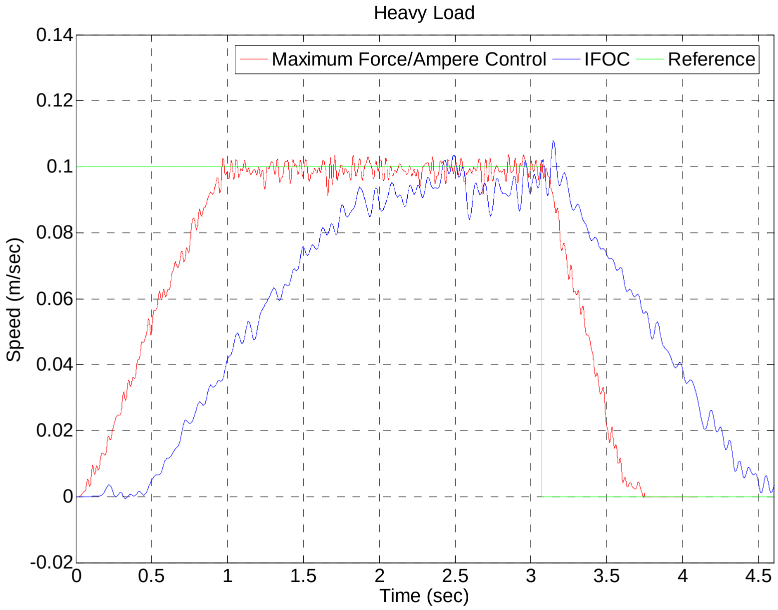

Figure 92 Speed Response of Both Methods (22 lbs Load)

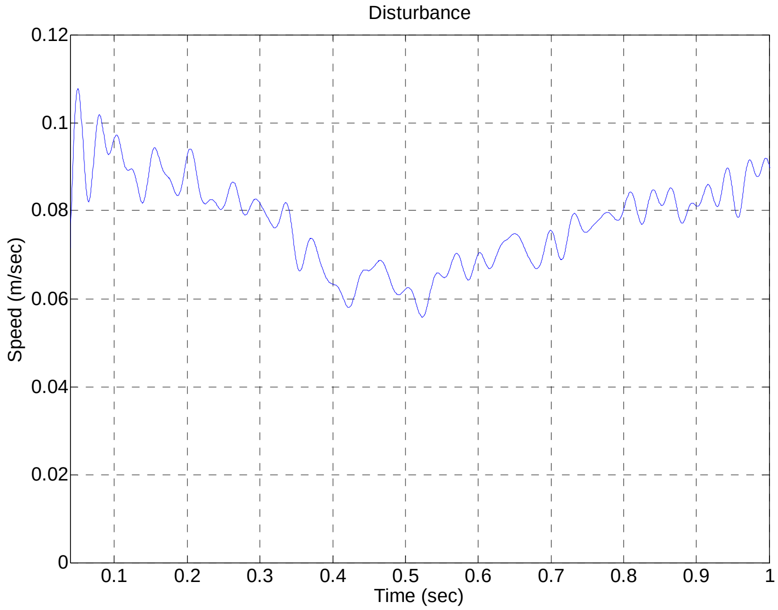

Figure 93 Speed Profile Subject to a Sudden Change of Load (22 lbs) Using IFOC

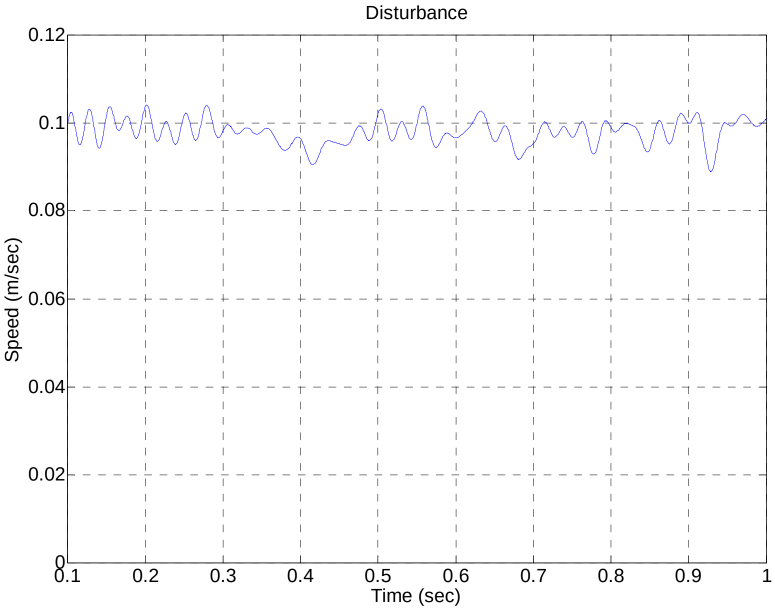

Figure 94 Speed Profile Subject to a Sudden Change of Load (22 lbs) Using Maximum Force/Ampere Control

CHAPTER 6

CONCLUSIONS AND FUTURTE RESEARCH

Linear induction machine (LIM) offers advantages such as easy maintenance, simple configuration, and high propulsive performance. Therefore, for the past few decades linear induction machines have been widely used in transportation, aerospace, and military. As a result, looking for a high grade control strategy has been a focal area. Vector control has been a preferred method of control in LIM because LIM possesses similarities from its rotary counterpart. However, some electromagnetic characteristics such as trailing eddy current effects and magnetic asymmetry effects have been proven to undermine the proper functionality of vector control for LIM. In addition, the investigation on airgap length effect, secondary electric conductivity effect, and back EMF characteristics has led to development of the in-depth knowledge of LIM electromagnetic behavior which results in further differences in the way these machines should be controlled. To address the need for an effective control, a new analysis method known as field reconstruction method (FRM) has been verified and applied in LIM. It is more computationally efficient than the traditional tool, i.e. finite element analysis. In the meantime, FRM also guarantees excellent computational accuracy. Thereafter, a new control scheme, maximum force/ampere control, is proposed in this dissertation. Maximum force/ampere control is simple, easy to implement, and fast technique. Both the simulation results and experimental test have validated the effectiveness of maximum force/ampere control.

On the basis of electromagnetic behavior, field reconstruction method, and maximum force per ampere control in the linear induction machines, the future research target should be focused on how to use FRM to detect faults in LIM and how to adopt a self healing mechanism that can seamlessly recover the drive in the event of a failure in one of the phases of the machine. Furthermore, advanced magnetic design approaches can benefit from the fast response of FRM. Finally, it will be desirable to combine the LIM with the magnetically levitated system (MagLev) to achieve ultra fast frictionless transportation, and optimize the design of LIM in the context of this application.

APPENDIX A

SPECIFICATIONS OF LIM

No.	Parameter	Description
01.	Type	Linear Induction Machine
02.	Power supply	240V, 3 phase AC
03.	Winding Configuration	wye
04.	Poles	4
05.	Slots per pole per phase	1
06.	Air Gap (mm)	2.5
07.	Primary Dimensions in x, y, and z Directions (mm)	250 x 72 x 100
08.	Reaction Plate Dimensions in x, y, and z Directions (mm)	1524 x 3 x 100
09.	Back iron Dimensions in x, y, and z Directions (mm)	1524 x 6 x 100
10.	Material of Primary Lamination	M19
11.	Material of Reaction Plate	Aluminum: 3.8e7 Siemens/meter
12.	Material of Back Iron	CR10: Cold rolled 1010 steel

APPENDIX B

LIM DRIVE SYSTEM

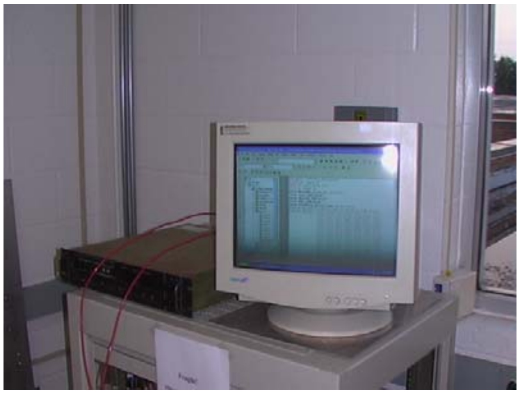

Control Station and DC Power Supply

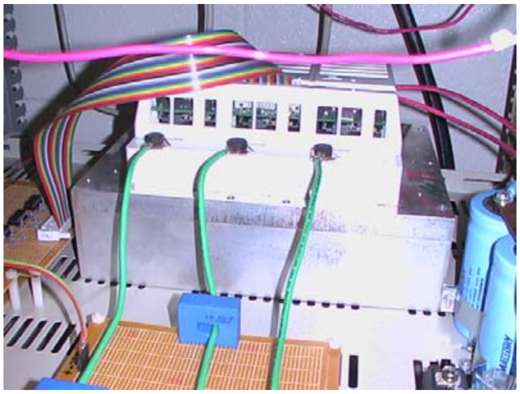

Three Phase IGBT Inverter

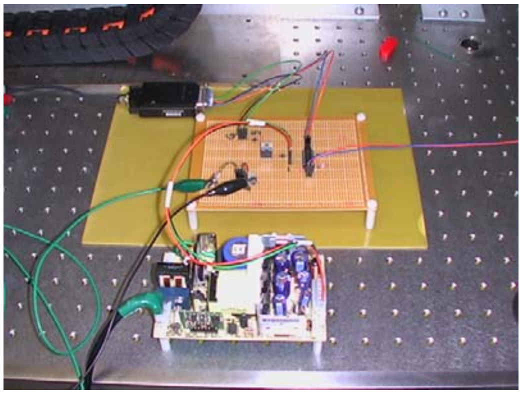

Interface and Protection Circuit of
Linear Position Encoder

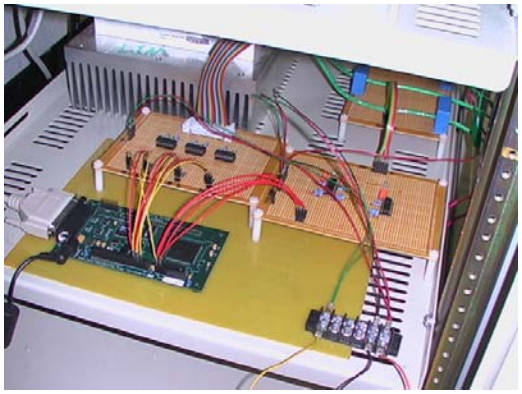

Control Board and ADC Circuit

REFERENCES

[1] I. Boldea, S. A. Nasar, “Linear Motion Electromagnetic System,” John Wiley & Sons Inc., 1995.

[2] S. A. Nasar, I. Boldea, “Linear Motion Electric Machines,” John Wiley & Sons Inc., 1976.

[3] E. R. Laithwaite, “Adapting a Linear Induction Motor for the Acceleration of Large Masses to High Velocities,” Electric Power Applications, IEE Proceedings, Volume 142, Issue 4, July 1995 Page(s): 262-268.

[4] D. J. De Groot, C. J. Heuvelman, “Tubular Linear Induction Motor for Use as a Servo Actuator,” Electric Power Applications, Volume 137, Issue 4, July 1990 Page(s): 273-280.

[5] M. I. Demsky, Yu. P. Vakhrusehin, A. E. Baranovsky, A. A. Volzhev, A. P. Luprianov, D. E. Trifonov, “Linear Induction Accelerators for Industrial Applications,” Particle Accelerator Conference, 1993., Proceedings of the 1993, 17-20 May 1993 Page(s): 682-684 vol.1.

[6] V. Di Dio, M. Montana, “State of Art of Tubular Linear Induction Motor,” Electrotechnical Conference, 1996. MELECON '96., 8th Mediterranean. Volume 1, 13-16 May 1996 Page(s): 285-288 vol.1.

[7] A. Munoz-Garcia, T. A. Lipo, D. W. Novotny, “A New Induction Motor V/F Control Method Capable of High-performance Regulation at Low Speeds,” IEEE Transactions on Industry Applications, Volume 34, Issue 4, July-Aug. 1998 Page(s): 813-821.

[8] S. Srilad, S. Tunyasrirut, T. Suksri, “Implementation of a Scalar Controlled Induction Motor Drives,” SICE-ICASE, 2006. International Joint Conference, Oct. 2006 Page(s): 3605-3610.

[9] I. Ludtke, M. G. Jayne, “Direct Torque Control of Induction Motors,” IEE Colloquium on Vector Control and Direct Torque Control of Induction Motors, 27 Oct. 1995 Page(s): 6/1-6/6.

[10] D. W. Novotny, T. A. Lipo, “Vector Control and Dynamics of AC Drives,” Oxford, U.K.: Clarendon, 1996.

[11] Byung-Il Kwon, Kyung-Il Woo, Sang-Woo Lee, Seung-Chan Park, “Experimental Investigations and Simulations Using FEM for the Direct Field Oriented Control of Linear Induction Motor,” Electric Machines and Drives Conference Record, 1997, IEEE International 18-21 May 1997 Page(s): MC1/10.1-MC1/10.3.

[12] E. F. Da Silva, E. B. Dos Santos, P. C. M. Machado, M. A. A. De Oliveria, “Vector Control for Linear Induction Motor,” Industrial Technology, 2003 IEEE International Conference on Volume 1, 10-12 Dec. 2003 Page(s): 518-523 Vol.1.

[13] Rong-Jong Wai, Chia-Chin Chu, “Indirect Field-Oriented Linear Induction Motor Drive with Petri Fuzzy-Neural-Network Control,” Neural Networks, 2005. IJCNN '05. Proceedings. 2005 IEEE International Joint Conference on Volume 1, 31 July-4 Aug. 2005 Page(s): 378-383 vol. 1.

[14] F.-J. Lin, C.-C. Lee, “Adaptive Backstepping Control for Linear Induction Motor Drive to Track Periodic References,” Electric Power Applications, IEE Proceedings- Volume 147, Issue 6, Nov. 2000 Page(s): 449-458.

[15] R.-J. Wai, F.-J. Lin, S.-P. Hsu, “Intelligent Backstepping Control for Linear Induction Motor Drive,” Control Theory and Applications, IEE Proceedings-Volume 148, Issue 3, May 2001 Page(s): 193-202.

[16] A. K. Rathore, S. N. Mahendra, “Simulation of Secondary Flux Oriented Control of Linear Induction Motor Considering Attraction Force & Transverse Edge Effect,” Power Electronics Congress, 2004. CIEP 2004. 9th IEEE International 17-22 Oct. 2004 Page(s): 158-163.

[17] G. Kang, K. Nam, “Field-Oriented Control Scheme for Linear Induction Motor with the End Effect,” Electric Power Applications, IEE Proceedings-Volume 152, Issue 6, 4 Nov. 2005 Page(s): 1565-1572.

[18] Jeong-Hyoun Sung, Kwanghee Nam, “A New Approach to Vector Control for a Linear Induction Motor Considering End Effects,” Industry Applications Conference, 1999. Thirty-Fourth IAS Annual Meeting. Conference Record of the 1999 IEEE Volume 4, 3-7 Oct. 1999 Page(s): 2284-2289 vol.4.

[19] S. Vaez-Zadeh, M. R. Satvati, “Vector Control of Linear Induction Motors with End Effect Compensation,” ICEMS 2005. Proceedings of the Eighth International Conference on Electrical Machines and systems, 2005. Volume 1, 27-29 Sept. 2005 Page(s): 635-638 Vol. 1.

[20] H. Yu, R. Jayabalan, M. Krishnamurthy, B. Fahimi, “Analysis of High Speed Characteristics for Linear Induction Machines,” Vehicle Power and Propulsion Conference, 2006. VPPC’06. IEEE 6-8 Sept. 2006 Page(s): 1-6.

[21] H. Yu, B. Fahimi, “An Investigation on Asymmetry Effects in Linear Induction Machines,” Applied Power Electronics Conference, APEC 2007-Twenty Second Annual IEEE Feb. 2007 Page(s): 390-395.

[22] V. Ostovic, “Computer Aided Analysis of Electric Machine,” Prentice Hall International, UK, 1994.

[23] K. Adamisk, J. Mizia, G. E. Dawton, A. R. Eastham, "Finite Element Force Calculation in Linear Induction Machines," IEEE Transactions on Magnetics, Vol. 1. No. 5. Sep. 1987.
[24] G. E. Dawson, A. R. Eastham, J. F. Gieras, "Design of Linear Induction Drives by Fields Analysis and Finite-element Techniques," IEEE Transactions, 1986, IA-22, (5), pp. 865-873.
[25] M. A. Al-Maayouf, S. R. Alwash, M. F. Bouniya, "Finite Element Analysis of Linear Induction Motors," Proc. International Conference on Electric Machine (ICEM), Page(s): 260-266, Munchen, 1986.
[26] W. Zhu, B. Fahimi, and S. Pekarek, "A Field Reconstruction Method for Optimal Excitation of Permanent Magnet Synchronous Machines", IEEE Transactions on Energy Conversion, vol. 21, no. 2, pp. 305-313, June 2006.
[27] D. Wu, S. D. Pekarek, B. Fahimi, "A Field Reconstruction Technique for Efficient Modeling of the Fields and Forces within Induction Machines," IECON 2007, Taiwan.
[28] P. C. Krause, O. Wasynczuk, S. D. Sudhoff, "Analysis of Electric Machinery," IEEE Press, 1995.
[29] I. V. Lindell, B. Jancewicz, "Maxwell Stress Dyadic in Differential-form Formalism," IEE Proceedings - Science, Measurement and Technology, Volume 147, Issue 1, Jan. 2000 Page(s):19-26.
[30] Z. Ren, A. Rezek, "Force Calculation by Maxwell Stress Tensor in 3D Hybrid Finite Element-boundary Integral Formulation," IEEE Transactions on Magnetics, Volume 26, Issue 5, Sep 1990 Page(s): 2774-2776.

BIOGRAPHICAL INFORMATION

Haidong Yu received his Bachelor of Engineering from Shandong University, China, in 2003, and M.Sc. in Power Electronics and Motor Drives from the University of Nottingham, UK, in 2005. He completed Ph.D. in Electrical Engineering in the University of Texas at Arlington. His research interest includes power electronics, motor drives, and power quality.